UV-Emitting Upconversion-Based TiO_2 Photosensitizing Nanoplatform: Near-Infrared Light Mediated *in Vivo* Photodynamic Therapy *via* Mitochondria-Involved Apoptosis Pathway

Zhiyao Hou,[†,§] Yuanxin Zhang,[†,§] Kerong Deng,[†,‡] Yinyin Chen,[†,‡] Xuejiao Li,[†] Xiaoran Deng,[†,‡] Ziyong Cheng,[†] Hongzhou Lian,[†] Chunxia Li,[*,†] and Jun Lin[*,†]

[†]State Key Laboratory of Rare Earth Resource Utilization, Changchun Institute of Applied Chemistry, Chinese Academy of Sciences, Changchun 130022, People's Republic of China and [‡]University of Chinese Academy of Sciences, Beijing 100049, People's Republic of China. [§]Z. Hou and Y. Zhang contributed equally.

ABSTRACT Photodynamic therapy (PDT) is a promising antitumor treatment that is based on the photosensitizers that inhibit cancer cells by yielding reactive oxygen species (ROS) after irradiation of light with specific wavelengths. As a potential photosensitizer, titanium dioxide (TiO_2) exhibits minimal dark cytotoxicity and excellent ultraviolet (UV) light triggered cytotoxicity, but is challenged by the limited tissue penetration of UV light. Herein, a novel near-infrared (NIR) light activated photosensitizer for PDT based on TiO_2-coated upconversion nanoparticle (UCNP) core/shell nanocomposites (UCNPs@TiO_2 NCs) is designed. $NaYF_4$:Yb^{3+},Tm^{3+}@$NaGdF_4$:Yb^{3+} core/shell UCNPs can efficiently convert NIR light to UV emission that matches well with the absorption of TiO_2 shells. The UCNPs@TiO_2 NCs endocytosed by cancer cells are able to generate intracellular ROS under NIR irradiation, decreasing the mitochondrial membrane potential to release cytochrome *c* into the cytosol and then activating caspase 3 to induce cancer cell apoptosis. NIR light triggered PDT of tumor-bearing mice with UCNPs@TiO_2 as photosensitizers can suppress tumor growth efficiently due to the better tissue penetration than UV irradiation. On the basis of the evidence of *in vitro* and *in vivo* results, UCNPs@TiO_2 NCs could serve as an effective photosensitizer for NIR light mediated PDT in antitumor therapy.

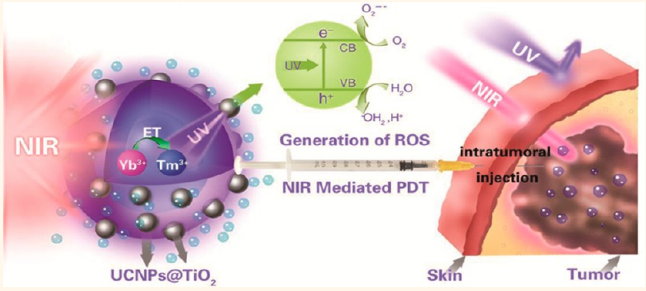

KEYWORDS: upconversion nanoparticles · titanium dioxide · core/shell structure · NIR light mediated · photodynamic therapy · mitochondria-involved apoptosis

Photodynamic therapy (PDT), a noninvasive and mild medical technique based on the photochemical reactions of photosensitizers (PSs) to generate cytotoxic intracellular reactive oxygen species (ROS), has undergone extensive investigations in cancer treatment.[1−6] PDT is an emerging and pioneering cancer therapeutic modality to improve the drawbacks of other traditional anticancer therapies. As the most widely used semiconductor, titanium dioxide (TiO_2) with the crystalline phase of anatase can absorb ultraviolet (UV) light to catalyze the generation of ROS.[7,8] Due to their irradiation-induced phototoxicity, UV light excited TiO_2 nanoparticles (NPs) of various sizes and morphologies are being investigated mainly in the phototherapy of malignant cells.[9−14] In comparison with traditional organic photosensitizers, TiO_2 NPs can be maintained for a longer time in the body, and they are nontoxic and stable without light irradiation. A major challenge in PDT is the direct illumination of the tissue by UV or visible light to trigger the PSs (including TiO_2 NPs). UV or

* Address correspondence to jlin@ciac.ac.cn (J. Lin), cxli@ciac.ac.cn (C. Li).

Received for review October 27, 2014 and accepted February 18, 2015.

Published online February 18, 2015
10.1021/nn506107c

visible light has a limited penetration distance in tissue, causing PDT to fail in cases where the cancer cells are located far from the surface.[15−20] Studies on the optical window in biological tissues reveal that the maximum penetration into tissue exists in the near-infrared (NIR) range (700−1000 nm).[21,22] Thus, NIR light triggered TiO_2 NPs will be potential and desirable PDT photosensitizing agents.

Upconversion processes generate a higher energy light from a lower energy light, typically NIR light.[23−29] Upconversion nanoparticles (UCNPs) based on lanthanide-doped nanocrystals, which could convert NIR light to UV or visible photons,[30−36] are able to activate the attached PSs *via* fluorescence resonance energy transfer (FRET) to generate ROS.[37−42] NIR light triggered UCNPs potentially open new doors to a next generation of photodynamic therapy. The current UCNP-based NIR light triggered PDT systems mainly focus on designing second-generation photosensitizers (mainly organic PSs) to efficiently utilize the upconverted light in the green and red emission regions of Yb/Er-co-doped UCNPs.[43−47] However, the TiO_2 NPs that could be triggered by UV light are usually ignored for inhibiting *in vitro* cancer cells, especially for the suppression of *in vivo* tumors, due to the low penetration into tissue and the damage to normal tissue, even though they possess high photosensitization activity toward various cancer cell lines. ROS generation of NIR light irradiated TiO_2 NPs is dependent on the energy transfer efficiency, which relies on the spectral overlap between the upconversion emission of UCNPs and the absorption of TiO_2 NPs. Yb/Tm-co-doped UCNPs, converting NIR light to UV emission that matches well with the absorption of TiO_2 NPs, may solve the above problem. Nevertheless, Yb/Tm-co-doped UCNPs with TiO_2 were mainly limited to photocatalytic activity *via* NIR light irradiation.[48−51] A new attempt at NIR light mediated PDT especially *in vivo* applications by employing Yb/Tm-co-doped UCNPs with enhanced UV emission as donors to trigger TiO_2 has not been explored.

Herein, we report a multifunctional cancer therapy nanoplatform for NIR light mediated and imaging guided PDT. The core/shell-structured $NaYF_4$:Yb^{3+},Tm^{3+}@$NaGdF_4$:Yb^{3+} UCNPs present enhanced upconverting UV emission in comparison with the original $NaYF_4$:Yb^{3+},Tm^{3+}, as well as the properties of MR and CT imaging. Crystallized shells composed of TiO_2 NPs were coated on the surface of $NaYF_4$:Yb^{3+},Tm^{3+}@$NaGdF_4$:Yb^{3+} cores to form ($NaYF_4$:Yb^{3+},Tm^{3+}@$NaGdF_4$:Yb^{3+})@TiO_2 core/shell nanocomposites (denoted as UCNPs@TiO_2 NCs). UCNPs@TiO_2 NCs can efficiently generate intracellular ROS *via* 980 nm NIR laser excitation to induce apoptotic cancer cell death *in vitro*. Compared to previous UCNP-based organic PS PDT systems, the novelty of our current study involves the following. (1) UCNPs@TiO_2 NCs with good biocompatibility and water dispersibility can serve as NIR light activated PS without introducing other cytotoxic organic PSs. The covalent linking of TiO_2 as a PS by themselves with high loading can effectively prevent PS molecules from leaking and self-aggregating. (2) As the donors, core/shell UCNPs can provide enhanced upconverting UV emission to trigger the acceptor TiO_2. Meanwhile, TiO_2 shells were coated directly on the surfaces of UCNPs, ensuring maximum energy transfer from UCNPs to TiO_2 so as to facilitate the generation and release of ROS. (3) The protein expression levels of apoptosis-related genes elucidate the possible molecular mechanisms of cancer cell inhibition. UCNPs@TiO_2-based NIR light mediated PDT can induce cancer cell death through a mitochondria-involved intrinsic apoptosis pathway. The expression activity of caspase 3 in tumor tissue could be enhanced after NIR light mediated PDT so as to induce the apoptosis of cancer cells and inhibit the growth of tumor *in vivo*. More importantly, owing to the deeper tissue penetration of NIR light than UV light, UCNPs@TiO_2-based NIR light mediated PDT possesses more effective tumor inhibition in comparison with UV light irradiated UCNPs@TiO_2.

RESULTS AND DISCUSSION

Synthesis and Characterization of UCNPs@TiO_2 NCs. The synthetic route for UCNPs@TiO_2 core/shell nanocomposites can be summed up into four steps, as presented in Figure 1a. The original $NaYF_4$:Yb^{3+},Tm^{3+} core with the mean diameter of 25 nm (Figure 1b) was synthesized by a thermal decomposition method, followed by being coated with the active shell $NaGdF_4$:Yb^{3+} on the surface through a seed-mediated process to obtain $NaYF_4$:Yb^{3+},Tm^{3+}@$NaGdF_4$:Yb^{3+} core/shell structured UCNPs (Figure 1c). After decorating ligand-free UCNPs with polyvinylpyrolidone (PVP), TiF_4 served as a Ti precursor to form TiO_2 shells on the surface of the UCNPs under mild hydrolysis conditions. From Figure 1d, it can be seen that the TiO_2 NPs are attracted onto the surface of the $NaYF_4$:Yb^{3+},Tm^{3+}@$NaGdF_4$:Yb^{3+} UCNPs to form UCNPs@TiO_2 core/shell NCs. The low-magnification high-angle annular dark field scanning TEM (HAADF-STEM) image further confirms the core/shell structure of the UCNPs@TiO_2 (Figure 1e), clearly showing the contrast between the shell (dark) and core (bright). The elemental mapping images were utilized to analyze the elemental distribution of the nanocomposites, as shown in Figure 1f. The results indicate that Ti and O elements are distributed in the shell, while Na and F are distributed in the core. For the distribution of rare earth (RE) elements in the $NaYF_4$:Yb^{3+},Tm^{3+}@$NaGdF_4$:Yb^{3+} UCNPs, Gd element is mainly distributed in the $NaGdF_4$:Yb^{3+} active shell, and the other RE elements are distributed in the $NaYF_4$:Yb^{3+},Tm^{3+} original core. From the corresponding low-magnification TEM images, high-resolution TEM (HRTEM) images, and

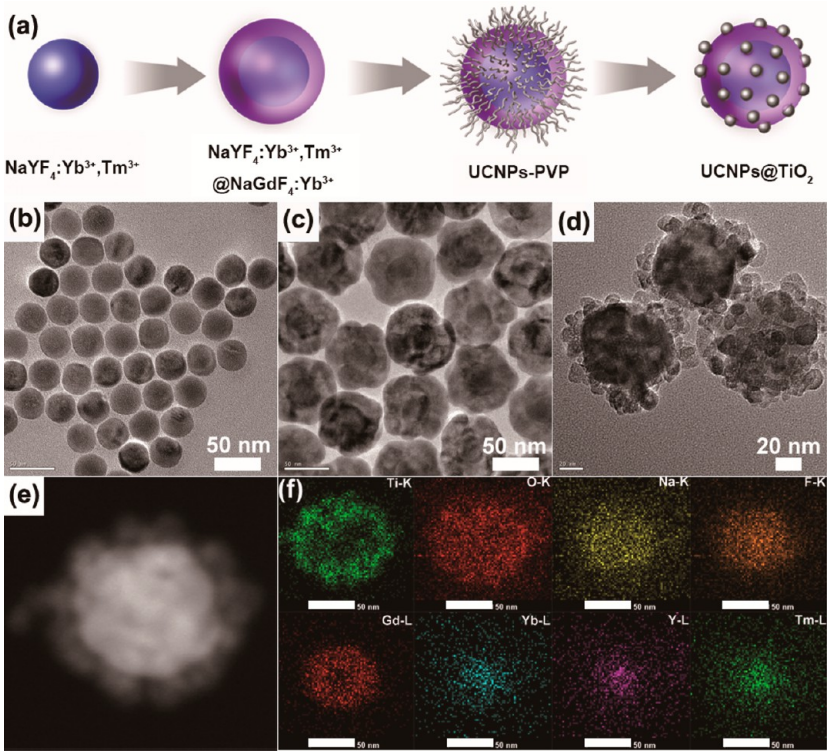

Figure 1. Schematic illustration for the synthetic procedure of UCNPs@TiO_2 NCs (a). TEM images of the original $NaYF_4$:Yb^{3+}, Tm^{3+} cores (b). $NaYF_4$:Yb^{3+},Tm^{3+}@$NaGdF_4$:Yb^{3+} core/shell UCNPs (c) and $NaYF_4$:Yb^{3+},Tm^{3+}@$NaGdF_4$:Yb^{3+}@TiO_2 (UCNPs@TiO_2) core/shell NCs (d). High-angle annular dark field scanning transmission electron microscopy (HAADF-STEM) image (e) and HAADF-STEM-EDS mapping image (f) of a single UCNPs@TiO_2 nanoparticle (all scale bars in (f) are 50 nm).

dynamic light scattering data (Figure S1), the above samples possess uniform morphology, good monodispersity, and high crystallinity. As a key role of the successful TiO_2 coating, PVP was capped onto the surface of core/shell ligand-free UCNPs to provide stable coating sites between UCNPs cores and TiO_2 NPs. PVP can coordinate lanthanide ions through pyrrolidone groups coated on the surface of the UCNPs.[52−54] PVP, hydrophilic polymers, can homogeneously stabilize UCNPs in the water/ethanol mixed solvent.[55−57] On the other hand, coating PVP is essential for stabilizing the TiF_4 on the surface of UCNPs to form the TiO_2 NPs (Figure S2a). Without the PVP coating, no continuous TiO_2 NPs were formed on the surface of the UCNPs (Figure S2b). With a very small amount of TiF_4 coated on the surface of UCNPs, the aggregation of self-nucleated TiO_2 samples can be observed. The one-step PVP-mediated protocol is a simple and general approach to synthesize core/shell TiO_2 nanocomposites through hydrothermal deposition of polycrystalline anatase TiO_2 NPs on the inorganic nanomaterials with different morphologies and sizes.[58−61] The structure of as-formed UCNPs@TiO_2 NCs was also characterized by X-ray diffraction (XRD) (Figure S3), and the red diffraction peaks can be ascribed to anatase TiO_2 phase (JCPDs 21-1272) besides the characteristic peaks of UCNPs (JCPDs 16-0334), indicating the successful coating of TiO_2 shells.

The obtained samples with good dispersibility emit upconverting light in UV/visible regions *via* 980 nm NIR

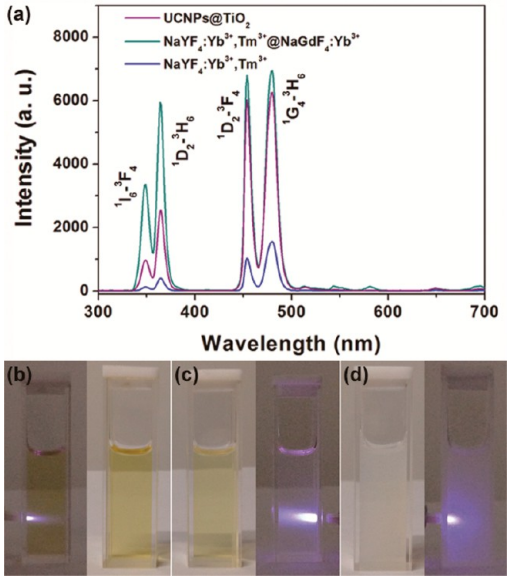

Figure 2. Upconversion emission spectra of $NaYF_4$:Yb^{3+}, Tm^{3+}, $NaYF_4$:Yb^{3+},Tm^{3+}@$NaGdF_4$:Yb^{3+}, and UCNPs@TiO_2 (a). Digital and luminescence photographs of $NaYF_4$:Yb^{3+},Tm^{3+} dispersed in cyclohexane (b), $NaYF_4$:Yb^{3+}, Tm^{3+}@$NaGdF_4$:Yb^{3+} dispersed in cyclohexane (c), and UCNPs@TiO_2 dispersed in water (d).

laser excitation (Figure 2). The UV emission peaks of Tm^{3+} ions can be derived from radioactive transitions of $^1I_6 \rightarrow {}^3F_4$ (348 nm) and $^1D_2 \rightarrow {}^3H_6$ (365 nm), and the visible emission can be assigned to $^1D_2 \rightarrow {}^3F_4$ (453 nm)

and $^1G_4 \rightarrow {}^3H_6$ (480 nm) transitions of Tm^{3+} ions, respectively.[48] Due to the suppressed surface quenching of bare $NaYF_4$, the relative emission intensity of core/shell $NaYF_4$:Yb^{3+},Tm^{3+}@$NaGdF_4$:Yb^{3+} UCNPs is about 15 times that of the original $NaYF_4$:Yb^{3+},Tm^{3+} core under similar measurement conditions. After coating TiO_2 shells outside the UCNPs cores with enhanced upconverting emission, all the emission peaks of UCNPs become weaker. Especially, the emission intensity of the UV region is remarkably diminished due to the absorbance of UV emission light by the TiO_2 shells.[49] To demonstrate the photocatalytic activities of the TiO_2 shells being formed on the UCNPs, the photocatalytic decomposition of methylene blue (MB) was carried out by the UCNPs@TiO_2 NCs under 365 nm UV light and 980 nm NIR laser irradiation (as shown in Figure S4), respectively. Obviously, the characteristic absorption bands of MB decreased steadily with the increase in irradiation time. The MB was degraded completely for UCNPs@TiO_2 NCs after 5 h of UV irradiation, and almost 50% of the MB was degraded with 5 h of NIR laser excitation, indicating that TiO_2 shells possess perfect photocatalytic activity toward MB.

ROS Generation of UCNPs@TiO_2 NCs *via* NIR Irradiation. Cytotoxic intracellular ROS can cause damage to DNA and mitochondria in cells, resulting in cell death.[62] Therefore, the ability to generate extracellular and intracellular ROS of the photosensitizer is one of the crucial factors that determine the efficacy of PDT. The generation of extracellular ROS, which was caused by the UCNPs@TiO_2 upon 980 nm NIR laser excitation, was detected by the chemical probe 1,3-diphenylisobenzofuran (DPBF) first. DPBF can react with ROS irreversibly and then causes the intensity of its characteristic absorption to decrease to 420 nm (Figure 3a). The absorbance of DPBF decreased exponentially with the increasing NIR illumination time, with approximately 85% decrease in 30 min, confirming the efficient generation of extracellular ROS.

The primary condition of intracellular ROS generation is effective cellular uptake of UCNPs@TiO_2 NCs. The incubation times were optimized to confirm the time required for the maximum amount of cellular uptake by HeLa cells. Cellular uptake of UCNPs@TiO_2 NCs was determined using inductively coupled plasma mass spectrometry (ICP-MS) and flow cytometry (FCM), respectively. ICP-MS were used to determine the titanium content in the cell lysis solution. As shown in Figure S5A, the mass of titanium internalized in HeLa cells from UCNPs@TiO_2 increased with the initial 6 h of incubation, and the titanium content decreased at the 7 and 12 h incubation time points. The cellular uptake degree of the UCNPs@TiO_2 NCs could be quantified with FCM by determining the green fluorescent signals of fluorescein isothiocyanate (FITC, fluorescent dye)-labeled UCNPs@TiO_2 NCs (UCNPs@TiO_2−FITC) treated

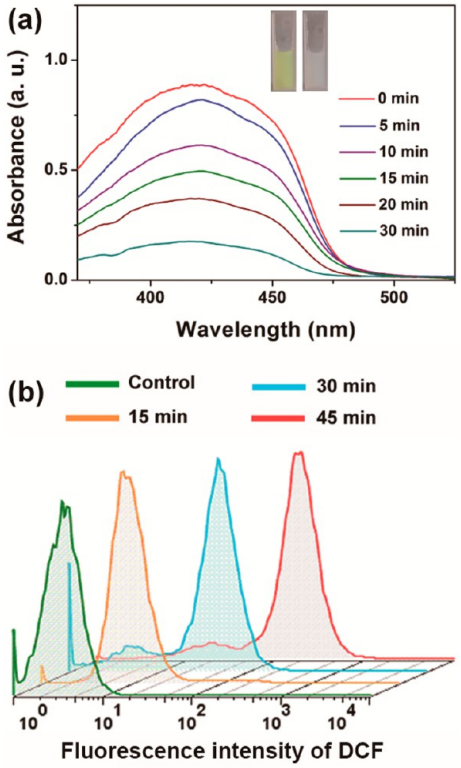

Figure 3. (a) Absorbance changes of DPBF treated with UCNPs@TiO_2 NCs after 980 nm laser irradiation for different times (inset: digital photographs of DPBF mixing with UCNPs@TiO_2 before (left) and after (right) irradiation). (b) Intracellular ROS generation was detected in HeLa cells treated with UCNPs@TiO_2 NCs under 980 nm laser irradiation. The level of intracellular ROS was measured by FACSCalibur flow cytometry using the peroxide-sensitive fluorescent probe DCFH-DA.

with HeLa cells (Figure S5B). The efficiency of cell uptake increased gradually with the extension of the incubation time, while the cellular uptake amounts at 6 and 7 h of incubation had no significant change. Combined with the above results, the optimal incubation time is 6 h. TEM is another effective means to verify cellular uptake and the location of UCNPs@TiO_2 NCs relative to the cells *in vitro*, and TEM measurements were done after 6 h of incubation (Figure S5C). As presented in Figure S5C(c) and (d), the UCNPs@TiO_2 NCs can be internalized by cells and then enter the lysosome or accumulate around the mitochondria. A TEM image of HeLa cells incubated with UCNPs@TiO_2 NCs *via* 980 nm NIR laser irradiation is shown in Figure S5C(b), presenting the changes in cell morphologies compared to a blank control cell (Figure S5C(a)). These changes include blebbing, cell shrinkage, chromatin condensation, and cytoplasm density increase. The above *in vitro* data provide direct evidence that the uptake of the UCNPs@TiO_2 NCs is achieved by endocytosis. After incubation with UCNPs@TiO_2 NCs in the dark, the HeLa cells were irradiated with a 980 nm laser and intracellular ROS formation was monitored *via* conversion of nonfluorescent 2,7-dichlorofuorescin

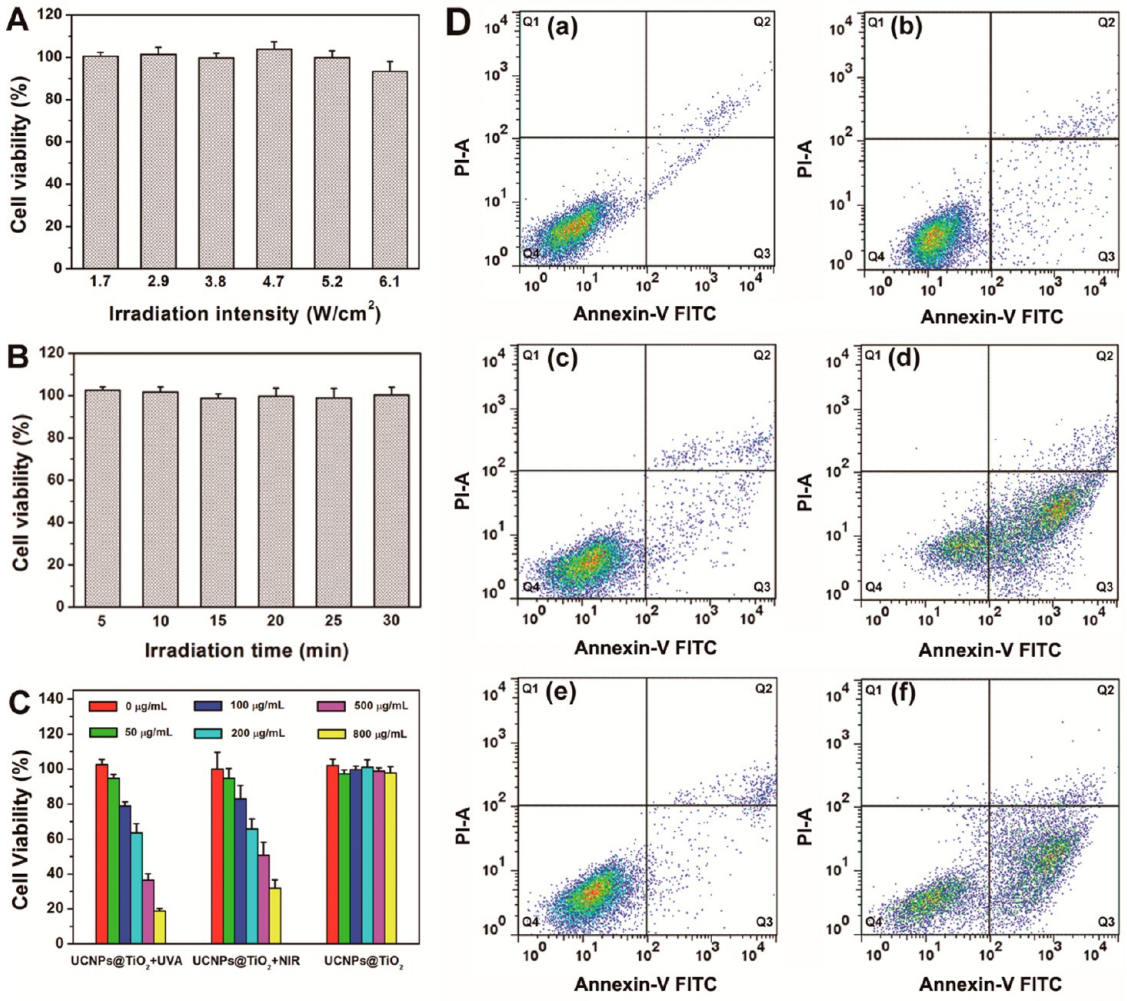

Figure 4. (A) Cell viability after being irradiated with a 980 nm laser under different intensities for 30 min (5 min break after 10 min of irradiation). (B) Cell viability after irradiation with 365 nm UV light under different irradiation times. (C) *In vitro* viabilities of HeLa cells treated with UCNPs@TiO_2 NCs under 365 nm UV light irradiation, 980 nm NIR laser irradiation, and no irradiation. Error bars indicate standard deviations, $n = 3$. (D) Apoptosis of HeLa cells by staining with annexin V-FITC and PI: (a) control, (b) UCNPs@TiO_2 NCs alone, (c) 365 nm UV light irradiation alone, (d) UCNPs@TiO_2 + 365 nm UV light irradiation, (e) 980 nm NIR laser irradiation alone, (f) UCNPs@TiO_2 + 980 nm NIR laser irradiation.

diacetate (DCFH-DA) to fluorescent dichlorofluorescein (DCF). The relative intracellular fluorescence intensity analyzed by FCM allows quantitative comparison of the ROS generation with different irradiation times (Figure 3b). There was no ROS produced when there was no irradiation, and the fluorescence intensity from DCF increased with increasing illumination time. Thus, UCNPs@TiO_2 NCs can serve as promising photosensitizers for NIR light triggered PDT.

***In Vitro* Anticancer Effect Induced by UCNPs@TiO_2 NCs in NIR-Triggered PDT.** The focus of this study aims to explore UCNPs@TiO_2 NCs as a PDT agent for the development of a NIR light triggered photodynamic inactivation system as a promising anticancer strategy. In order to confirm the safety of the cells, the phototoxicity of the 980 nm NIR laser and 365 nm UVA light was investigated first, and the cytotoxicity results were estimated using the MTT assay. The short-interval irradiation prevented the culture medium from being overheated, and the 980 nm NIR laser irradiation (5 min break after 10 min of irradiation) showed no significant cytotoxic effects on the HeLa cells (Figure 4A). Moreover, 365 nm UV light irradiation with different irradiation times also did not affect the growth of HeLa cells (Figure 4B). Thus, the light excitation has no toxic effects on the cells. To confirm the PDT efficacy of UCNPs@TiO_2 NCs in HeLa cells, the cytotoxic effects of UCNPs@TiO_2 NCs on HeLa cells under 980 nm NIR laser and 365 nm UV light irradiation are presented in Figure 4C. HeLa cells only with the UCNPs@TiO_2 NCs acted as the control. The UCNPs@TiO_2 without any light excitation had no impact on cell viability over a wide range of concentrations, suggesting a low dark toxicity, thus ensuring a large potential range of applications in the field of cancer photodynamic therapy. However, the viability of the HeLa cells treated with UCNPs@TiO_2 in the

presence of 980 nm laser (4.7 $W \cdot cm^{-2}$, 5 min break after 10 min of irradiation) or 365 nm light irradiation for 30 min decreased remarkably compared to those under light irradiation or UCNPs@TiO_2 alone, which indicated that the phototoxicity of UCNPs@TiO_2 could have increased the mortality of HeLa cells. Thus, the cell death was dominated by the NIR light triggered PDT effect resulting from the fluorescence resonance energy transfer from UCNP cores to TiO_2 shells upon 980 nm NIR laser excitation. Additionally, we also prepared core/shell NCs by directly coating the original $NaYF_4:Yb^{3+},Tm^{3+}$ core with a TiO_2 shell (Figure S6). The survival rate of HeLa cells treated with $NaYF_4:Yb^{3+}$, Tm^{3+}@TiO_2 is obviously higher than those with UCNPs@TiO_2 treatment *via* 980 nm laser irradiation, indicating lower PDT efficacy due to the ineffective upconvering of the NIR laser to UV emission of $NaYF_4:Yb^{3+}$, Tm^{3+} compared to $NaYF_4:Yb^{3+},Tm^{3+}$@$NaGdF_4:Yb^{3+}$. Thus, to improve the efficacy of TiO_2-based NIR light mediated PDT, it is necessary to coat the $NaGdF_4:Yb^{3+}$ active shell outside the original $NaYF_4:Yb^{3+},Tm^{3+}$ core.

Cell death pathways of PDT include apoptosis, necrosis, and autophagy-associated cell death.[63] To detect the pathway of cell death induced by NIR light triggered PDT, the effect of UCNPs@TiO_2 on apoptotic death in HeLa cells was assessed by employing annexin V/PI staining and FACS analysis, as shown in Figure 4D. Flow cytometry with annexin V (annexin V-FITC) and PI staining can clearly distinguish early apoptosis from late apoptosis or necrosis. As indicated in FACS analysis scatter grams, annexin V/PI staining of control cells and UCNPs@TiO_2 alone showed a large viable cell population with very few staining for early apoptotic, late apoptotic, and dead cells. However, comparing with light irradiation, which caused no significant apoptosis, NIR or UV light mediated PDT treatment of HeLa cells with UCNPs@TiO_2 at 500 $\mu g \cdot mL^{-1}$ doses resulted in a stronger shift from live cells to early apoptotic and late apoptotic cell populations. The dose- and irradiation time-dependent apoptotic effects of NIR-triggered UCNPs@TiO_2 in HeLa cells are clearly shown in Figure S7. All the results indicated that apoptosis was a major cell death modality in HeLa cells responding to NIR light triggered PDT with the UCNPs@TiO_2 NCs.

Cell Apoptosis Mechanisms for NIR-Triggered PDT. Two main apoptotic pathways have been documented: death receptor-mediated apoptosis (extrinsic pathway) and mitochondria-mediated apoptosis (intrinsic pathway). Mitochondria have emerged as the central processing organelles in the majority of apoptotic pathways. Mitochondria membrane potential (MMP, $\Delta\Psi m$) is an early event in apoptosis, and JC-1 staining was used to evaluate the alterations in $\Delta\Psi m$.[64−66] When the $\Delta\Psi m$ is high, JC-1 accumulates in the mitochondrial matrix to form JC-1 aggregates that produce red fluorescence. Alternatively, green fluorescence is generated by the JC-1 monomers when JC-1 cannot assemble in the mitochondrial matrix. As presented in Figure S8, in the HeLa cells incubated with UCNPs@TiO_2 alone, a high MMP was maintained, as indicated by the predominantly red fluorescence of the JC-1 aggregates. However, after 980 nm NIR light irradiation PDT treatment, the intensity of the red fluorescence of JC-1 aggregates was significantly weaker and the green fluorescence of JC-1 monomers was stronger compared with the control group (Figure 5A). To further confirm the above results, HeLa cells were treated with UCNPs@TiO_2 with and without NIR light irradiation, stained with JC-1, followed by flow cytometry (Figure 5B). FCM results showed control cells, UCNPs@TiO_2 alone, and NIR light alone with well-polarized, red-emitting mitochondria localized in the upper region of the plot, revealing no mitochondrial damage. HeLa cells treated with NIR light mediated PDT underwent a progressive loss of red fluorescence, and a shift downward over different irradiation times indicated a loss of MMP and mitochondrial damage. The change in the microscopy or cytofluorimetric pattern suggests that NIR light mediated PDT can induce apoptosis through a mitochondria-involved apoptosis pathway. To investigate the underlying molecular mechanism for the induction of apoptosis by NIR light mediated PDT, the protein expression of Bcl-2 family proteins in UCNPs@TiO_2-treated HeLa cells after a 30 min irradiation with a 980 nm laser was measured by Western blotting, as shown in Figure 5C. The activation of mitochondria is controlled by the family of Bcl-2 proteins, which are classified as proapoptotic proteins (*e.g.*, Bax and Bak) and antiapoptotic proteins (*e.g.*, Bcl-2, Bcl-xL, and Mcl-1).[67,68] After NIR light mediated PDT, increased levels of Bak (Figure S9a) but no obvious modulation of Bax (Figure S9b) were observed. In parallel, the expressions of Bcl-xL (Figure S9c) and Bcl-2 (Figure S9d) were significantly decreased and no significant difference in Mcl-1 protein expression (Figure S9e) between the control and PDT group was observed. The overexpression of Bcl-xL has been detected in many human cancers,[69] and down-regulation of Bcl-xL was found in the mitochondria-involved apoptosis.[70] Up-regulation of Bak can form multimers and lead to cytochrome *c* release from mitochondria into the cytosol to promote cell apoptosis.[71−73] Chiang and co-workers discovered a significantly higher expression of Bak protein in oral verrucous hyperplasia and oral leukoplakia lesions treated with topical 5-aminolevulinic acid-mediated photodynamic therapy (ALA-PDT).[74,75] They concluded that the Bak and the ratio of the proapoptotic to antiapoptotic protein (Bak/Mcl-1) may serve as important biomarkers that can predict the clinical outcome of topical ALA-PDT. In addition, antiapoptotic proteins (Bcl-2, Bcl-xL, and Mcl-1) can counteract the proapoptotic activity from Bax, and the ratio of Bax/Bcl-2 might be another useful factor in the cell threshold for undergoing apoptosis induced by PDT.[76−78] The increased levels in the ratios of Bak/Bcl-xL, Bak/Mcl-1,

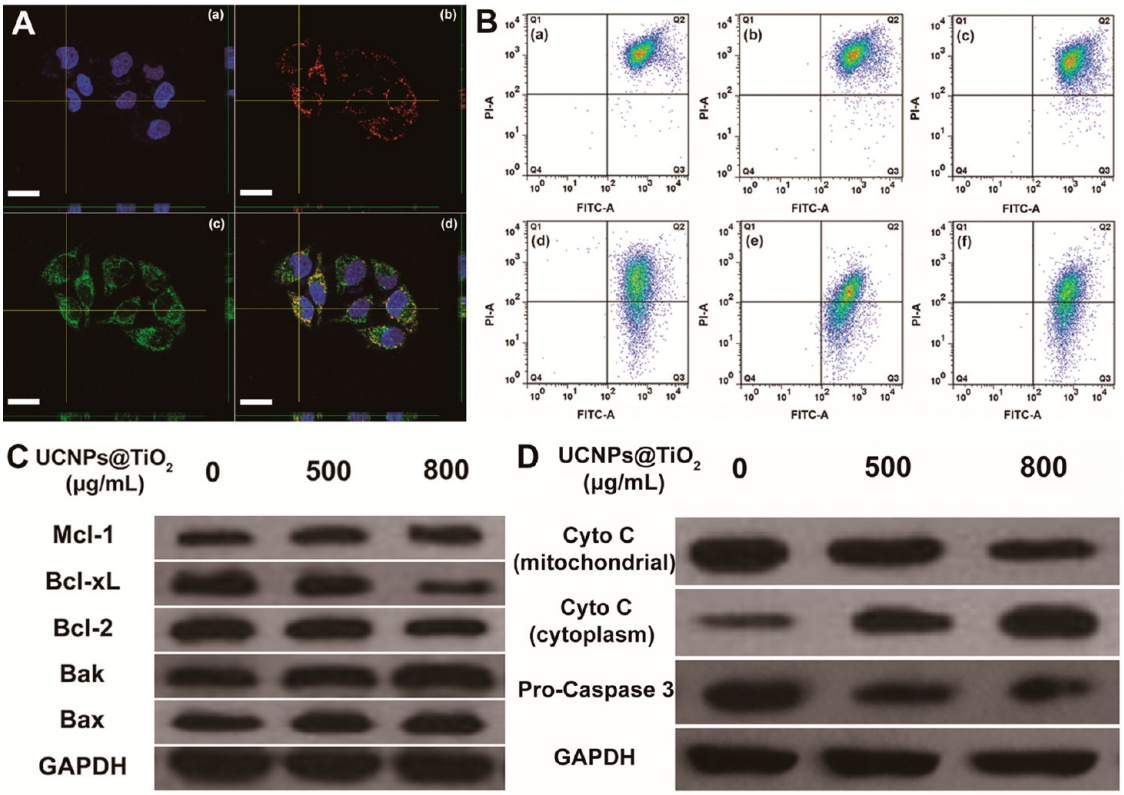

Figure 5. NIR-mediated PDT induced mitochondrial damage in HeLa cells. (A) Cells treated with UCNPs@TiO_2 NCs (800 $\mu g \cdot mL^{-1}$) were irradiated by a 980 nm laser (4.7 $W \cdot cm^{-2}$, 30 min, 5 min break after 10 min of irradiation) and stained with JC-1. Increase of green fluorescence in irradiated cells suggests loss of mitochondrial membrane potential: (a) nuclei of cells being dyed blue by Hoechst 33324, (b) JC-1 forming red-emitting aggregates in the mitochondrial matrix, (c) green-emitting monomers in the cytoplasm, (d) overlapped image, *x*−*y* top view at a given *z*, and two other images of the respective *x*−*z* and *y*−*z* side views along the green lines. All scale bars are 30 μm. (B) The change of mitochondria membrane potential was objectively measured using flow cytometry: (a) control, (b) UCNPs@TiO_2 NCs alone, (c) 980 nm NIR laser irradiation alone, (d−f) UCNPs@TiO_2 + 980 nm NIR laser irradiation for different times (10, 20, and 30 min). (C) Expression of Bcl-2 family proteins (*i.e.*, Bax, Bak, Bcl-2, Bcl-xL, and Mcl-1) by Western blotting analysis after 30 min of irradiation using a 980 nm laser; GAPDH was used as an internal control. (D) Expression of Cyto C and pro-caspase 3 proteins by Western blotting analysis after 30 min irradiation using a 980 nm laser; GAPDH was used as an internal control.

and Bax/Bcl-2 demonstrated NIR light mediated PDT has proapoptotic effects on HeLa cells (Figure S10). The levels of cytochrome *c* in the cytoplasm were significantly increased, together with a corresponding decline of cytochrome *c* in the mitochondria (Figure 5D), revealing the release of cytochrome *c* from mitochondria into the cytoplasm. Cytochrome *c*, a pivotal effector of apoptosis, can lead to the activation of caspases in the apoptosome. Caspase 3 is the main effector caspase that is involved in apoptosis. The expression of pro-caspase 3 decreased significantly after NIR light mediated PDT treatment (Figure S9f). To identify whether caspase 3 is involved in NIR-mediated PDT induced apoptosis, the catalytic activity of caspase 3 was measured using a caspase colorimetric assay kit. Caspase activity was significantly increased compared to the control group after NIR-mediated PDT treatment (Figure S11a), indicating the activation of caspase 3. To further evaluate the role of caspase 3 in the apoptosis pathway, HeLa cells were pretreated with the caspase 3 inhibitor Ac-DEVD-CHO before PDT treatment. Pretreatment of Ac-DEVD-CHO can attenuate cell death efficiently following NIR-mediated PDT treatment (Figure S11b). The above results revealed that the NIR-mediated PDT induced apoptosis can be through a caspase-dependent mechanism.

The potential molecular mechanism of inducing apoptosis with UCNPs@TiO_2-based NIR light mediated PDT treatment is summarized in Scheme 1. Irradiated by the 980 nm NIR laser, the UCNPs cores upconvert NIR light to UV light and transfer it to the TiO_2 shells. The electron on the valence band of the TiO_2 shell was excited to the conduction band, and a hole was generated on the valence band, resulting in the formation of an electron−hole pair, eliciting further redox reactions for the generation of ROS (such as H_2O_2 and $OH^{\bullet}$). Intracellular ROS, which were generated by UCNPs@TiO_2 accumulated in the membranes of mitochondria *via* NIR light irradiation, induce mitochondrial inner membrane permeabilization and depolarization. Often the first event observed in PDT-induced apoptosis is a dissipation of the MMP. The members of the Bcl-2 family proteins are the key regulators of the mitochondria-mediated apoptosis.[79,80] Bcl-2 protein

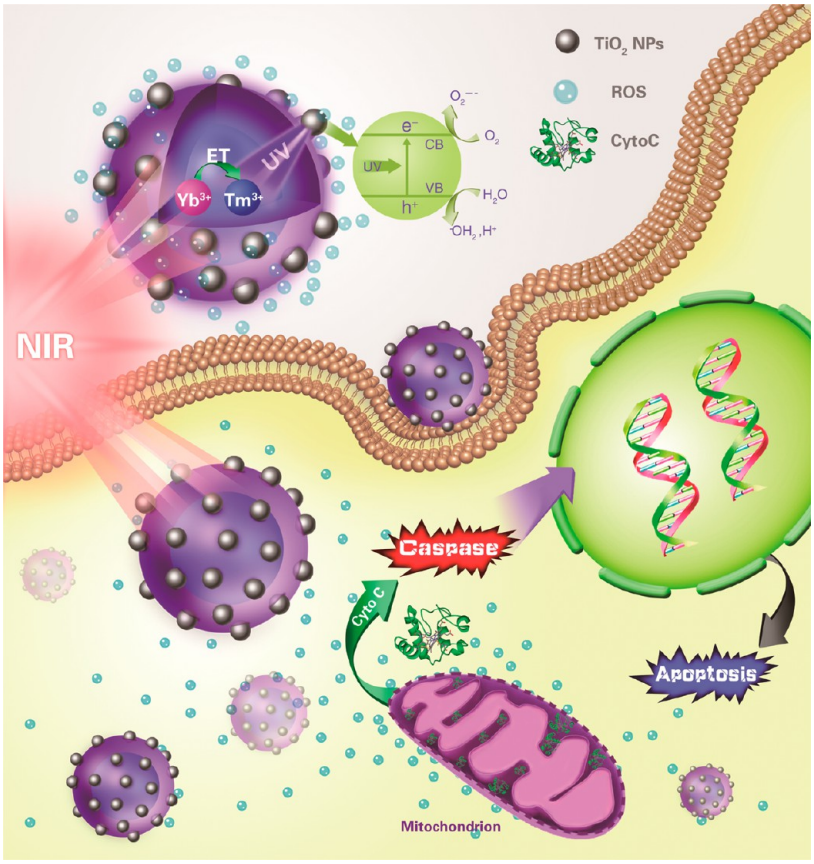

Scheme 1. Plot for potential molecular mechanism of inducing apoptosis with UCNPs@TiO_2-based NIR light mediated PDT treatment.

expression was proposed to be associated with a favorable response to PDT and could be used as a predictor of cancer response to PDT. NIR light mediated PDT based on UCNPs@TiO_2 induces selective down-regulation of the proapoptotic proteins (Bcl-xL and Bcl-2) and up-regulation of antiapoptotic protein (Bak), as well as the increased levels of Bak/Bcl-xL, Bak/Mcl-1, and Bax/Bcl-2. The major influence over a cell's propensity to undergo apoptosis in response to a toxic stimulus is the ratio of the antiapoptotic proteins to proapoptotic proteins. As the switch of mitochondria-related apoptosis, the shift in the balance between the activities of proapoptotic and antiapoptotic proteins can decide the susceptibility of cells to PDT-mediated apoptosis. Thus, the increase of the Bak/Bcl-xL, Bak/Mcl-1, and Bax/Bcl-2 ratios might be a critical factor in the HeLa cell threshold for undergoing apoptosis induced by UCNPs@TiO_2 NCs as PS in NIR-mediated PDT. Cytochrome *c* (one of apoptogenic molecules) is a pivotal effector during apoptosis;[81−83] the release of cytochrome *c* from mitochondria is a key step in PDT-induced apoptotic death. The intrinsic, mitochondrial apoptotic pathway is regulated by the Bcl-2 family proteins that govern the release of cytochrome *c* from the mitochondria. The up-regulation of Bak protein can promote the release of cytochrome *c* from the mitochondria into the cytosol, initiating the apoptotic cascade. NIR light mediated PDT treatment significantly increased the levels of cytochrome *c* in the cytoplasm, together with a corresponding decline of mitochondrial cytochrome *c*. In the cytosol, cytochrome *c* probably binds with Apaf-1 and pro-caspase 9, leading to the activation of pro-caspase 9 in the oligomeric complex (the apoptosome). Caspase 9 cleaves and activates the pro-caspase 3 (downstream caspases). The level of pro-caspase 3 decreased significantly after NIR light mediated PDT treatment, indicating the activation of caspase 3. Caspase 3, the major executioner caspase, is activated in most cases of PDT-induced apoptosis with a number of different photosensitizers.[84−86] The activation of caspase 3 results in the biochemical and morphological features of apoptotic cell death, including cell shrinkage, membrane blebbing, and internucleosomal DNA fragmentation. All the above results suggest that the induction of apoptosis in UCNPs@TiO_2-treated HeLa cells by NIR light mediated PDT may be associated with the disruption of mitochondrial function and activation of caspases.

***In Vivo* Tumor Inhibition Efficacy.** To investigate the imaging-guided therapeutic potential *in vivo*, a HeLa tumor model was selected to evaluate the antitumor efficacy of UCNPs@TiO_2-based NIR light mediated PDT, as well as the MR and CT imaging effects. In addition to enhancing upconverting emission, the $NaGdF_4$:Yb^{3+} active shell also plays an important role in improving

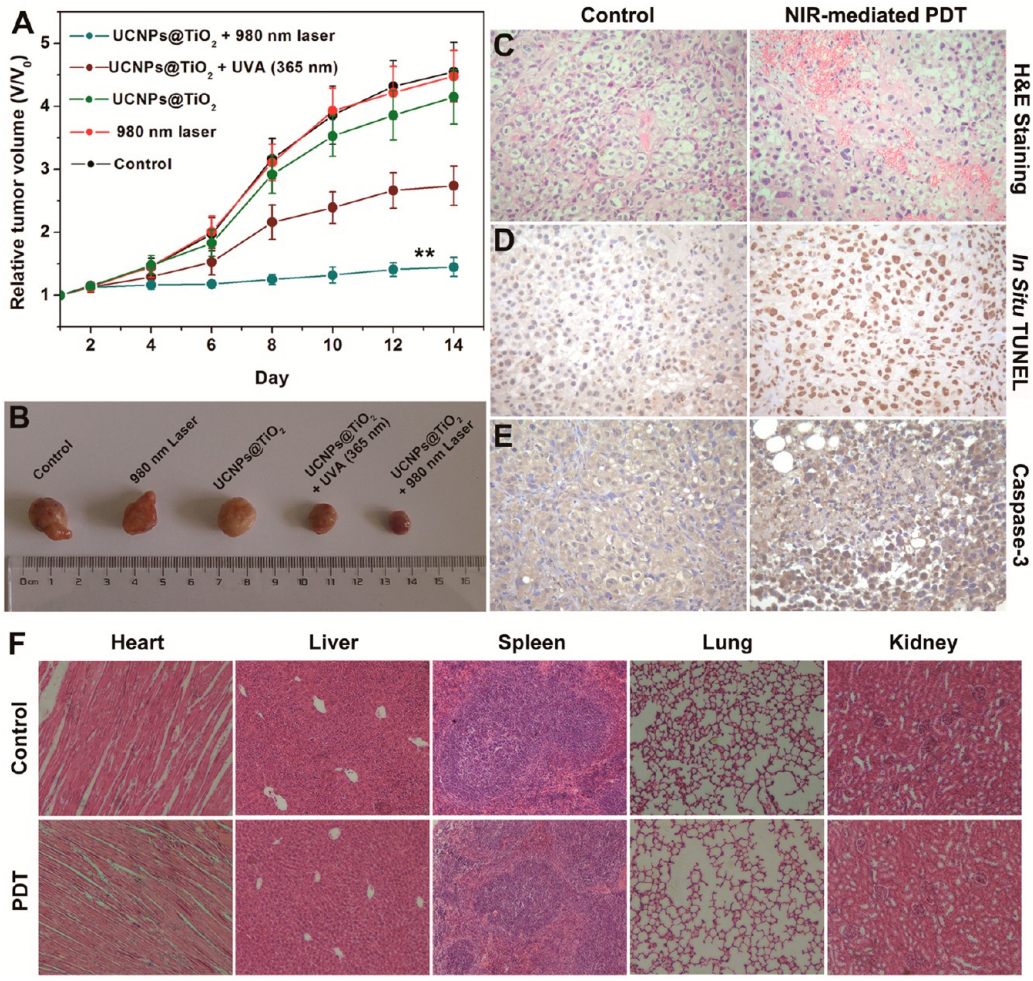

Figure 6. *In vivo* **tumor volume changes of tumor-bearing mice in different groups after various treatments (A); error bars indicate standard deviations,** $n = 6$ (**$p < 0.01$ **as compared with the control group). Digital photographs of excised tumors from representative mice after various treatment (B). Images of H&E stained tumor sections from the control group and NIR light mediated PDT group (C). Representative images of the tumor sections examined by TUNEL assay (D). Representative photographs of the tumor sections examined by immunohistochemical staining for caspase 3. The assessment of caspase 3 was based on a cytoplasmic staining pattern (E). Representative histological H&E staining of various organ tissues from the control group and NIR light mediated PDT group (F). (Original magnification: C, D, and E, 200×; F, 80×.)**

MRI and CT sensitivity. T_1-weighted MR images of UCNPs and UCNPs@TiO_2 acquired by a 1.2 T MR scanner revealed the concentration-dependent brightening effects (Figure S12a). Compared with UCNPs at the same concentration of Gd, the UCNPs@TiO_2 presented a little lower positive contrast enhancement due to the TiO_2 shell coating outside the UCNPs. The longitudinal relaxivity (r_1) values of UCNPs and UCNPs@TiO_2 are 0.8634 and 0.6873 mM^{-1} s^{-1}, respectively (Figure S12b). *In vivo* MR imaging of tumor-bearing mice was further performed by intratumorally injecting a solution of UCNPs@TiO_2 NCs. As illustrated in Figure S12c and d, the tumor site shows a little higher MRI signal intensity after injection, revealing that the UCNPs@TiO_2 NCs may serve as a potential contrast agent for T_1 MR imaging. For high-resolution and deep tissue penetration, X-ray CT is an important diagnostic imaging technique. The CT contrast efficacy of Yb- and Gd-based UCNPs@TiO_2 core/shell NCs was assessed. The CT values and signals increased with increasing the concentration of the UCNPs@TiO_2 NCs (Figure S13a,b). *In vivo* CT imaging was further detected by intratumorally injecting a solution of UCNPs@TiO_2 NCs. The CT value in the tumor increases from 25 Hounsfield units (HU) to 178 HU at coronal position (Figure S13c,f), confirming that UCNPs@TiO_2 core/shell NCs could serve as a contrast agent for CT imaging to monitor the UCNPs@TiO_2 locating in the tumor during the process of PDT. HeLa tumor-bearing Balb/c nude mice were intratumorally injected with UCNPs@TiO_2 NCs (Figure S14a), and the tumor sites were irradiated by a 980 nm laser at 12 h postinjection (Figure S14b). The groups that received intratumorally injected saline and UCNPs@TiO_2 without subsequent laser exposure served as controls. In addition, mice that received 980 nm laser irradiation without intratumoral injection were also applied as a control. The tumor volume in the control group increased remarkably during the

treatment, as shown in Figure 6A. In sharp contrast, the group treated with 980 nm laser irradiated UCNPs@TiO_2 showed a much slower growth rate, indicating the good tumor growth inhibition efficacy (Figure S14c,d). The digital photos of excised tumors from representative mice (Figure 6B) visually display that the tumor sizes under NIR light mediated PDT treatments were smaller than the other groups (Figure S15). Moreover, the group with UCNPs@TiO_2 intratumorally injected *via* 980 nm laser irradiation exhibited better tumor inhibition than that under 365 nm light irradiation due to the deeper tissue penetration of NIR light than UV light. Liu and co-workers loaded chlorin e6 (Ce6) onto $NaFY_4$-based UCNPs to form a UCNP−Ce6 complex, which is used for NIR light mediateded PDT treatment of tumors in an animal model, demonstrating the efficient NIR-induced PDT of tumors using UCNPs with intratumoral injection.[17] Yoon, Lee, and Hyeon prepared $NaYF_4$:Yb,Er/$NaGdF_4$ core/shell nanoparticles with enhanced upconversion emission and conjugated Ce6 on the UCNPs to induce a therapeutic effect. They demonstrated the PDT effect of UCNP−Ce6 through systemic administration *via* 980 nm laser irradiation.[90] The above excellent research provided an encouraging alternative to circumvent limitations of current photodynamic therapies. On the basis of the previous experiences of the reported research, we designed a novel NIR light activated photosensitizer for PDT based on UCNPs@TiO_2 without introducing other cytotoxic organic PSs, and NIR light triggered PDT of tumor-bearing mice with an intratumoral injection of UCNPs@TiO_2 can suppress tumor growth efficiently. Histological analysis showed that little damage was found in the tumor tissues from the control group, whereas most of tumor tissue cells under NIR light mediated PDT treatments were destroyed, as evidenced by the images of hematoxylin and eosin (H&E) staining of tumor slices (Figure 6C). To further confirm the ability of NIR light mediated PDT to elicit apoptosis *in vivo*, *in situ* TUNEL staining was carried out on tissue sections of tumors excised from the mice treated with 980 nm laser irradiated UCNPs@TiO_2.[87−89] As illustrated in Figure 6D, UCNPs@TiO_2-based NIR light mediated PDT caused a significantly higher percentage of TUNEL-positive apoptotic cells (dark brown nuclei) than the control group. Further, to verify whether regression in tumor growth by NIR light mediated PDT was due to induction of apoptosis, we studied expressions of caspase 3 in PDT treatment tumor samples and observed that NIR-mediated PDT enhanced the expression of caspase 3 protein (more caspase 3 staining in the cytoplasm) as compared to the control tumors (Figure 6E). Representative images with low magnification of the tumor sections examined by H&E staining (A), TUNEL assay (B), and immunohistochemical staining for caspase 3 (C) are presented in Figure S16. The result was similar to the *in vitro* NIR light mediated PDT. We also looked into the potential toxic side effects of the UCNPs@TiO_2-based NIR light mediated PDT treatment. Histology analysis of major organs from mice after UCNPs@TiO_2 injection and NIR light mediated PDT treatment indicated no appreciable abnormality or noticeable organ damage (Figure 6F). All the results preliminarily proved that the UCNPs@TiO_2-based NIR light mediated and bioimaging-guided PDT could be a safe and practical cancer treatment technique.

CONCLUSION

In summary, we reported an efficient NIR light mediated photosensitizing nanoplatform for PDT based on UCNPs@TiO_2 core/shell NCs. UCNPs@TiO_2 could efficiently produce extracellular and intracellular ROS by converting deeply penetrating NIR light into UV light to excite the TiO_2 shell attached on the UCNPs core. On comparing with the original $NaYF_4$:Yb^{3+},Tm^{3+} core, $NaYF_4$:Yb^{3+},Tm^{3+}@$NaGdF_4$:Yb^{3+} core/shell structured UCNPs could transfer the enhanced upconverting UV light to the TiO_2 shell, which inhibited tumor cells more effectively. *In vitro* anticancer results suggest that the induction of apoptosis in UCNPs@TiO_2-treated cells by NIR light mediated PDT may be associated with disruption of mitochondrial function and activation of caspases. The results of *in vivo* PDT clearly indicate that the approach of an indirectly exciting TiO_2 shell *via* a 980 nm NIR laser is more effective in practical tumor inhibition than direct excitation of UCNPs@TiO_2 with 365 nm UV light due to the higher tissue penetration depth of NIR light. On the basis of the evidence of *in vitro* and *in vivo* studies, we provide a NIR light mediated strategy for *in vivo* PDT with UCNPs@TiO_2. In addition, due to the presence of Gd and Yb ions in the UCNPs@TiO_2 NCs, these NCs could serve as potential MRI and CT contrast agents, which may monitor the physiological procedures in cancer treatment. Therefore, UCNPs@TiO_2 with efficient PDT effects and good imaging capability are a promising multifunctional cancer therapy nanoplatform for simultaneous bioimaging and therapeutics.

MATERIALS AND METHODS

Materials. All the chemical reagents were used as received without further purification. Rare earth oxides (Y_2O_3, Gd_2O_3, Yb_2O_3, and Tm_2O_3) were purchased from the Science and Technology Parent Company of the Changchun Institute of Applied Chemistry (China). Octadecene (ODE, 90%, technical grade), oleic acid (OA, 90%, technical grade), polyvinylpyrrolidone (PVP, M_w = 40,000), fluorescin isothiocyanate (FITC), and aminopropyltrimethoxysilane (APTMS) were purchased from Aldrich. Ammonium fluoride (NH_4F) was purchased from Beijing

Yili Fine Chemical Regent Company (China). TiF_4 (99%) was purchased from Acros. The rare earth chlorides YCl_3, $YbCl_3$, and $ErCl_3$ were prepared by dissolving the corresponding rare earth oxides in hydrochloric acid at elevated temperature followed by evaporating the solvent.

Synthesis of $NaYF_4$:Yb^{3+},Tm^{3+}@$NaGdF_4$:Yb^{3+} Core/Shell UCNPs. $NaYF_4$:Yb^{3+},Tm^{3+} (59.5% Y^{3+}, 40% Yb^{3+}, and 0.5% Tm^{3+}, molar ration) parent cores were prepared *via* a thermal decomposition reaction.[91] Our previously developed method was used to synthesize $NaYF_4$:Yb^{3+},Tm^{3+}@$NaGdF_4$:Yb^{3+} core/shell UCNPs.[92,93] In a typical procedure, after removing residual water and oxygen under vacuum with magnetic stirring, 20 mL of OA/ODE (v/v = 1:1) containing 2 mL of cyclohexane solution with half of the above parent cores was rapidly heated from 150 °C to 310 °C under a N_2 atmosphere. As the shell precursors, 1 mmol of $RE(CF_3COO)_3$ (98% Gd^{3+} and 2% Yb^{3+}, molar ratio) mixed with 4 mL of OA/ODE (v/v = 1:1) containing 1 mmol of CF_3COONa was injected into the above solution immediately. The reaction was kept 1 h at 310 °C, and the obtained oleic acid-stabilized $NaYF_4$:Yb^{3+},Tm^{3+}@$NaGdF_4$:Yb^{3+} core/shell structured UCNPs were dispersed in 15 mL of cyclohexane for further coating of TiO_2.

Synthesis of UCNPs@TiO_2 Core/Shell Nanocomposites. The above core/shell UCNPs, which were isolated by centrifuging a mixture of 1 mL of UCNP cyclohexane solution and excess ethanol, were transferred into 5 mL of a 0.05 M HCl solution. After ultrasonication to remove the surface ligands, ligand-free UCNPs were obtained *via* centrifugation. The ligand-free UCNPs were dispersed in 5 mL of deionized water containing 0.5 g of polyvinylpyrolidone (average mol wt 40 000) with ultrasonication and magnetic stirring for 1 h. Then these PVP-capped UCNPs were mixed with 20 mL of ethanol under magnetic stirring for another 30 min. As a titanium source, 4 mL of a 0.025 M TiF_4 aqueous solution was added dropwise into the above solution under stirring. The as-formed reaction solution was transferred into a 50 mL sealed Teflon-lined autoclave and maintained at 180 °C for 6 h. After cooling the autoclave to room temperature, the obtained precipitates were separated by centrifugation and washed with ethanol and deionized water three times, respectively. The as-synthesized UCNPs@TiO_2 core/shell NCs were sterilized by autoclaving and dispersed in bacteria-free water for further applications.

UV-Driven Photocatalysis Experiment. In a typical photocatalytic test, a mixture of 20 mg of UCNPs@TiO_2 core/shell NCs (catalyst) and 4 mL of methylene blue solution (5 mg·L^{-1}, dye) was kept in the dark for 12 h before irradiation. Then WD-9403E (8 W, 365 nm ultraviolet lamp, China) and KS3-11312-312 (2 W, 980 nm laser, BWT Beijing Ltd.) served as the irradiation sources. After irradiation for different times, 2 mL of the MB aqueous solution was withdrawn, followed by centrifugation. The concentration of MB in the supernatant was determined by UV−vis absorption spectrum at the characteristic wavelength 663 nm.

***In Vitro* Dark Cytotoxicity of UCNPs@TiO_2 NCs.** HeLa cells were plated out at a density of 5000 cells per well in a 96-well plate and incubated overnight to allow the cells to attach to the bottom of the wells. The ultrasonically treated UCNPs and UCNPs@TiO_2 were diluted in Dulbecco's modified Eagle's medium (DMEM) (containing 10% fetal bovine serum) at serial concentrations of 50, 100, 200, 500, and 800 $\mu g \cdot mL^{-1}$ and then added to the culture wells to replace the original culture medium for another 24 h, incubating at 37 °C. The MTT assay, a standard test for screening the toxicity of biomaterials in accordance with ASTM standards, was used on the HeLa cells to evaluate the relevant cell viabilities.

Cellular Uptake and Localization of UCNPs@TiO_2 NCs. Cellular uptake and localization of UCNPs@TiO_2 were examined using inductively coupled plasma mass spectrometry, flow cytometry, and TEM, respectively. HeLa cells (1×10^6) were seeded in six-well plates. These cells were treated with UCNPs@TiO_2 NCs (500 $\mu g \cdot mL^{-1}$) and then incubated at 37 °C for various times (1, 3, 5, 6, 7, and 12 h). After being rinsed with PBS three times, the cells were lysed by cell lysis buffer. ICP-MS was used to determine the titanium content in the cell lysis solution.

Fluorescein isothiocyanate was used to label UCNPs@TiO_2 (UCNPs@TiO_2−FITC) as follows: 2 mg of FITC and 45 μL of APTMS were dissolved in 1 mL of ethanol, and the mixture was stirred at room temperature for 12 h in the dark. Then 20 mg of composites dispersed in 20 mL of ethanol was added in 20 μL of the above solution, and the mixture was refluxed at 80 °C for another 12 h. The composites were separated by centrifugation and washed with ethanol and dialysis against water (cutoff molecular weight: 8000−10 000 Da). Cellular uptake by HeLa cells was examined using flow cytometry. For FCM studies, HeLa cells (1×10^6) were seeded in six-well culture plates and grown overnight. The cells were then treated with UCNPs@TiO_2−FITC (500 $\mu g \cdot mL^{-1}$) at 37 °C for 1, 2, 3, 5, 6, and 7 h. A single cell suspension was prepared consecutively by trypsinization, washing with PBS, and filtration through 35 mm nylon mesh. Thereafter, the cells were lifted using a cell stripper (Media Tech. Inc.) and analyzed using a FACSCalibur flow cytometer (BD Biosciences) for FITC. The excitation and emission wavelengths were 488 and 525 nm, respectively.

The HeLa cells were seeded in six-well culture plates at a density of 1×10^5 cells per well and incubated overnight, followed by incubation with UCNPs@TiO_2 NCs (500 $\mu g \cdot mL^{-1}$) for 6 h at 37 °C. Then, the cells were thoroughly washed with PBS in order to eliminate NCs that were not internalized. Subsequently, cells were trypsinized with trypsin, collected by centrifugation, fixed in glutaraldehyde (2.5%), embeded in resin, cut into ultrathin sections, stained by osmic acid, and finally imaged using TEM. Sections of fixed whole cells containing UCNPs@TiO_2 NCs were examined by a Hitachi H-7650 TEM (Japan) with a field emission gun operating at 80 kV.

Extracellular and Intracellular ROS Detection. The generation of extracellular ROS quantum yield was measured with a DPBF probe. In a typical process, 10 mg of UCNPs@TiO_2 NCs was dispersed well in 2 mL of DPBF solution (0.5 mg·mL^{-1}) with ultrasonic processing in the dark; then the mixture was irradiated, with magnetic stirring, under a 980 nm NIR laser (BWT Beijing Ltd., 4.7 W·cm^{-2}) for various time periods. The generation of ROS was demonstrated by the characteristic absorption decrease of the DPBF using a UV−vis absorption spectrum.

A cell-permeable dye of fluorogenic substrate DCFH-DA, which could be oxidized to the highly fluorescent DCF by ROS, was chosen to detect the intracellular generation of ROS. After a 6 h incubation of HeLa cells in the dark with UCNPs@TiO_2 NCs, noninternalized NCs were rinsed with PBS, and fresh culture media containing DCFH-DA (20 μm) was added for another 1 h incubation in the dark. The HeLa cells were then irradiated with a 980 nm NIR laser at a power density of 4.7 W·cm^{-2} for 30 min. To prevent the culture medium from being overheated, the laser treatment was done at 5 min intervals for each 10 min irradiation. A 980 nm NIR laser irradiated the entire area of the well, and the temperature of the culture medium in the well was monitored at the interval time points during the irradiation process. The temperature of the culture medium in the well increased from 22.5 °C to 29.3 °C after 10 min irradiation by the 980 nm laser and decreased to 23.6 °C 5 min after the laser was shut down. Then the irradiated cells were collected by trypsinization, resuspended in PBS after being washed three times, and filtered through 35 mm nylon mesh to form a single-cell suspension. The intracellular ROS level was analyzed using the FACSCalibur flow cytometer, where the gate was arbitrarily set for the detection of green fluorescent DCF. The excitation and emission wavelengths were 485 and 525 nm, respectively.

***In Vitro* PDT Effect.** The HeLa cells were seeded in 96-well culture plates at a density of 5000 cells per well. After being incubated overnight, the cells were treated with UCNPs@TiO_2 NCs at serial concentrations of 50, 100, 200, 500, and 800 $\mu g \cdot mL^{-1}$ for 6 h at 37 °C in the dark. After removing the medium containing noninternalized NCs, the cells were washed three times with PBS and then irradiated for 30 min with the 980 nm NIR laser (4.7 W·cm^{-2}, 5 min break after 10 min irradiation) and 365 nm UV light (0.52 W·cm^{-2}) in the fresh culture medium, respectively. After the PDT process, the cells were further incubated for 24 h in the dark, and the cell viability relative to the control untreated cells was evaluated using the MTT assay.

Annexin Flow Cytometry. After the NIR light triggered PDT treatment of UCNPs@TiO_2 NCs, HeLa cells were incubated for a further 3 h at 37 °C in the dark. Then cells (1×10^6) were harvested, washed twice with cold PBS (0.01 M, pH = 7.4), and

resuspended in binding buffer according to the manufacturer's protocols. Aliquots of the cells were mixed and incubated with annexin-V-FITC and PI for 15 min at room temperature in the dark. The induction of apoptosis was determined by analyzing 15 000 ungated cells using a FACScan cytometer and Cell Quest software (FACS Calibur; Becton-Dickinson, San Jose, CA, USA). All experiments were performed in triplicate.

Mitochondrial Membrane Potential Detection Using JC-1. As the hallmark for cellular apoptosis, MMP was measured using JC-1 (fluorescent cationic dye, 5,5′,6,6′-tetrachloro-1,1′,3,3′-tetraethylbenzimidazolylcarbocyanine iodide) by detecting a switch from red to green fluorescence. After NIR light triggered PDT treatment and a further 3 h incubation, HeLa cells (1×10^6) grown on a 35 mm confocal dish were washed twice with PBS and incubated with JC-1 dye in serum-free medium for 20 min at 37 °C. Subsequently, treated cells were rinsed with cold JC-1 buffer solution two times, incubated in fresh medium, and visualized under a laser confocal microscope. The images were detected at 488 nm excitation and 530 nm emission for green (JC-1 monomers) and at 543 nm excitation and 590 nm emission for red fluorescence (JC-1 aggregates). All the parameters used in confocal microscopy were kept constant in each sample. In addition, the percentage of low $\Delta\Psi$m cells was assessed by flow cytometry. JC-1-stained HeLa cells were suspended in PBS and analyzed using a FACSCalibur cytometer equipped with a 488 nm argon laser to assess the percentage of low $\Delta\Psi$m cells. The *x*-axis (FL-1 channel) of flow cytometry results indicated the green fluorescence intensity (JC-1 monomers), and the *y*-axis (FL-2 channel) was used to detect the red fluorescence (JC-1 aggregates). The region Q_2 encloses the low $\Delta\Psi$m cell population.

Cytosol/Mitochondria Fractionation. After NIR light triggered PDT, HeLa cells were harvested and then fractionated using a cytosol/mitochondria fractionation kit according to the supplier's recommendations. Briefly, cells were resuspended in an extraction buffer (20 mmol·L^{-1} 4-(2-hydroxyethyl)-1-piperazineethanesulfonic acid (HEPES, pH = 7.5), 1.5 mmol·L^{-1} $MgCl_2$, 10 mmol·L^{-1} KCl, 1 mmol·L^{-1} ethylenediaminetetraacetic acid, 1 mmol·L^{-1} ethylene glycoltetraacetic acid, 1 mmol·L^{-1} dithiothreitol, 0.1 mmol·L^{-1} phenylmethylsulfonyl fluoride, and 250 mmol·L^{-1} sucrose) and homogenized with a microhomogenizer. The homogenates were centrifuged at 500*g* for 10 min at 4 °C. The supernatants were centrifuged at 10000*g* for 15 min at 4 °C. The remaining supernatant was designated as the cytosol fraction, and the precipitation was mitochondria.

Total Protein Extraction. At the end of NIR light triggered PDT treatment, HeLa cells were washed twice with cold PBS and lysed for 30 min in 120 mL ice-cold cell-lysis buffer (50 mmol·L^{-1} Tris, pH = 8.0, 150 mmol·L^{-1} NaCl, 0.1% SDS, 1% NP40, and 0.5% sodium deoxycholate) containing proteinase inhibitors (1% Cocktail and 1 mmol·L^{-1} PMSF). Protein concentrations were determined *via* Bradford assay.

Western Blotting Analysis. Protein samples (30−50 μg) were denatured in 5× SDS-PAGE sample buffer and were subjected to SDS-PAGE on 12% Tris-glycine gels. The separated proteins were transferred onto 0.2 μm PVDF membranes for 2 h at 60 V using a Mini Trans-Blot electrophoretic transfer cell (Bio-Rad, Hercules, CA, USA). The membranes were blocked with 5% nonfat milk power (w/v) in TBST (10 mM Tris, 100 mM NaCl, and 0.1% Tween 20) for 1 h at room temperature. The specific primary antibodies (dilution ratio: 1:500) were used to probe the protein levels of the different desired molecules overnight at 4 °C, followed by the appropriate peroxidase-conjugated secondary antibodies (dilution ratio: 1:2000) for 2 h at room temperature. The blots were visualized by Western blotting detection reagents containing DL-p-Chloroamphetamine hydrochloride (PCA) and luminol according to the recommended procedure. After normalization with the corresponding expression of GAPDH, the protein expression was determined using densitometry scans. The data were expressed as the mean ± standard deviation ($n = 3$).

Caspase 3 Activity Assay. The activities of caspase 3 were determined by colorimetric assays using caspase 3 activation kits according to the manufacturer's protocols. At the end of the NIR light triggered PDT treatment, the HeLa cells were washed twice with cold PBS and scraped with a rubber policeman. Cells were centrifuged at 10000*g* at 4 °C, and the cell pellet was lysed in 100 μL of the supplied lysis buffer. The resulting suspension was centrifuged at 10000*g*, 4 °C, 10 min, and 10−20 μL of supernatant was used for the caspase assay. The supernatants were then collected and incubated at 37 °C, with the supplied reaction buffer, which contained dithiothreitol and substrates. The caspase 3 activity was then determined by measuring changes in the absorbance at 405 nm using a microplate reader.

Inhibitor Treatment. The cell culture was preincubated for 2 h with the caspase 3 specific inhibitor Ac-DEVD-CHO (100 μM) before the addition of UCNPs@TiO_2 NCs. At the end of the NIR light triggered PDT process, the cell viability was measured by the MTT assay to evaluate whether the NIR-mediated PDT was related to apoptosis through the caspase 3 pathway.

Animal Tumor Model and *in Vivo* PDT Treatment. The *in vivo* study conforms to the guidelines of the National Regulation of China for Care and Use of Laboratory Animals. Female Balb/c nude mice (6 weeks old, purchased from Center for Experimental Animals, Jilin University) were selected for establishing the xenograft HeLa tumor models. HeLa cells (4×10^6) in 100 μL of DMEM were subcutaneously injected into the armpit, and the tumors were allowed to grow to a uniform size of around 100−150 mm^3. The mice bearing HeLa tumors were randomly assigned into five groups ($n = 6$): (a) control (only received with saline), (b) 980 nm laser irradiation alone, (c) UCNPs@TiO_2 injection alone, (d) UCNPs@TiO_2 injection + 365 nm UV light irradiation for 30 min, (e) UCNPs@TiO_2 injection + 980 nm laser irradiation for 30 min. The tumors of group (b) were only irradiated with the 980 nm laser at a power density of 2.9 W·cm^{-2}. To avoid any tissue damage by heating, the laser treatment was done with a 5 min interval for each 10 min of irradiation. The surface temperature of the skin at the tumor site increased from 26.8 °C to 31.2 °C after 10 min of irradiation by the 980 nm laser and decreased to 27.2 °C after shutting down the laser for 5 min. Therefore, the short-interval NIR light irradiation is safe for the tissue. All the groups received only one intratumoral injection with 100 μL of UCNPs@TiO_2 (10 mg·mL^{-1}). Group (c) was only injected with UCNPs@TiO_2 in the dark as a control. For groups (d) and (e), at 12 h postinjection, the tumor sites were irradiated with UV light and the 980 nm laser, respectively. The body weights and tumor volumes were monitored every 2 days after PDT treatment, for up to 14 days. The tumor volume was calculated using the following formula: Tumor volume (V) = length × width^2/2. Relative tumor volume was calculated as V/V_0 (V_0 was the corresponding tumor volume when the treatment was initiated).

Histology Examination. For histology analysis, the mice were sacrificed 24 h post PDT treatment. Organs and tumor tissues from the control group and NIR PDT treated group were excised, fixed in 4% formalin overnight, and then embedded in paraffin. Tissue sections were deparaffinized in xylene, dehydrated in graded alcohols (100%, 95%, 85%, 75%), and washed in distilled water. The sliced tissue sections were stained with standard hematoxylin and eosin (H&E) staining and then analyzed with the inverted florescence microscope system (Nikon Ti-S).

***In Situ* TUNEL Assay for Apoptotic Cells.** Apoptotic cell death in paraffin-embedded tumor tissue sections was detected using the In Situ Cell Death Detection Kit (Roche Applied Science, Mannheim, Germany) according to the manufacturer's protocol. The paraffin samples were removed from the sections with xylene, rehydrated in graded alcohol series, and then placed in 3% hydrogen peroxide in methanol for 10 min at room temperature. Sections were then incubated with 20 mg·mL^{-1} proteinase K for 15 min. The sections were washed several times in PBS and then incubated with equilibration buffer for 15 s and TdT-enzyme at 37 °C for 1 h. Antibody blocking then proceeded for 5 min, and then anti-fluorescein antibody-POD (POD) (conjugated with horseradish peroxidase) was dropped on the slides. 3,3′-Diaminobenzidine (DAB) was used as the staining agent. Apoptotic cells were identified as dark brown nuclei under a light microscope.

Immunohistochemical Analysis. Immunohistochemical detection of caspase 3 in 5 μm thick tumor sections was performed. The tumor sections were hydrated in 1× PBS for 5 min.

The sections was incubated in 10 mM sodium citrate buffer for antigen retrieval (pH = 6.0, 80 °C, 10 min). The sections were cooled to room temperature, washed with 1× PBS for 5 min, and incubated in PBS containing 1% hydrogen peroxide for 5 min to block endogenous peroxidases. The sections were washed with 1× PBS for 5 min and blocked for 1 h in PBS containing 1.5% normal serum. The slides were then incubated with primary antibodies against caspase 3 (Santa Cruz, USA) at 4 °C in a humidified chamber. After washing with PBS, the sections were incubated with horseradish peroxidase-conjugated secondary antibodies (dilution ratio: 1:100) for 30 min at 37 °C. The immune reaction was visualized by color development with DAB. After counterstaining with hematoxylin, all sections were dehydrated, mounted with coverslips, and viewed under the inverted florescence microscope system (Nikon Ti-S, 100× magnification).

***In Vitro* and *in Vivo* T_1 Weighted MR Imaging.** The *in vitro* and *in vivo* MR imaging experiments were performed in a 1.2 T MRI instrument (Shanghai Sci&Edu of Shiming Globe Instrument Co. Ltd. HT-MRSI50-50KY). UCNPs@TiO_2 NCs with various concentrations of Gd (determined by ICP-MS) were dispersed in the water. T_1 was acquired using an inversion recovery sequence. T_1 measurements were performed using a nonlinear fit to changes in the mean signal intensity within each well as a function of repetition time by a 1.2 T MR scanner. The relaxivity values of r_1 were determined through the curve fitting of $1/T_1$ relaxation time (s^{-1}) *vs* the Gd concentration (mM). To perform *in vivo* MR imaging, UCNPs@TiO_2 NCs (100 μL, 10 mg·mL^{-1}) were intratumorally injected into the tumor-bearing mouse *in situ*. Then the tumor-bearing mouse was anesthetized with 10% chloral hydrate by intraperitoneal injection. The mouse was scanned before and after intratumoral injection.

***In Vitro* and *in Vivo* CT Imaging.** The CT imaging experiments were performed at a Siemens SOMATOM Sensation 64, and HU variations were acquired and analyzed using Syngo CT 2009S (Siemens, Berlin, Germany). The UCNPs@TiO_2 NCs with various concentrations were dispersed in PBS and placed in 1.5 mL tubes for *in vitro* CT imaging. To perform *in vivo* CT imaging, UCNPs@TiO_2 NCs (100 μL, 10 mg·mL^{-1}) were intratumorally injected into the tumor-bearing mouse *in situ*. Then the tumor-bearing mouse was anesthetized with 10% chloral hydrate by intraperitoneal injection. The mouse was scanned before and after intratumoral injection. *In vivo* CT images were acquired at predetermined time intervals with a slice thickness of 1.0 mm, a tube voltage of 120 kV, and an electrical current of 280 mA.

Statistical Analysis. Statistical analysis was performed with the Statistical Program for Social Sciences software (SPSS, Chicago, IL, USA) as needed. All data were expressed as means ± standard deviation, and a statistically significant difference was considered to be present at $p < 0.05$. Except as mentioned, all assays were repeated in triplicate in three independent experiments.

Conflict of Interest: The authors declare no competing financial interest.

Supporting Information Available: The Supporting Information file includes TEM images, XRD patterns, *in vitro* and *in vivo* T_1-weighted MR and CT images, photocatalytic activities, cellular uptake results, *in vitro* anticancer effect induced by $NaYF_4$:Yb^{3+},Tm^{3+}@TiO_2 in NIR-triggered PDT, apoptosis of UCNPs@TiO_2-treated HeLa cells induced by NIR-mediated PDT, confocal laser scanning microscopy images of HeLa cells stained with JC-1, representative immunohistochemical staining quantitative analysis of proteins, effect of NIR-mediated PDT on caspase 3 activity in HeLa cells, the survival of HeLa cells after NIR-mediated PDT treatment with caspase-3 inhibitor, digital photographs of tumor sections after cancer therapy, tumor volumes and weights of the excised tumors from mice in each group, representative images with low magnification of the tumor sections examined by H&E staining, TUNEL assay, and immunohistochemical staining for caspase 3. This material is available free of charge *via* the Internet at http://pubs.acs.org.

Acknowledgment. This project is financially supported by the National Natural Science Foundation of China (NSFC 51472233, 51332008, 51422209, 51372243) and National Basic Research Program of China (2014CB643803).

REFERENCES AND NOTES

1. Dougherty, T. J.; Kaufman, J. E.; Goldfarb, A.; Weishaupt, K. R.; Boyle, D.; Mittleman, A. Photoradiation Therapy for the Treatment of Malignant Tumors. *Cancer Res.* **1978**, *38*, 2628–2635.
2. Bonnett, R. Photosensitizers of the Porphyrin and Phthalocyanine Series for Photodynamic Therapy. *Chem. Soc. Rev.* **1995**, *24*, 19–33.
3. Dolmans, D. E. J. G. J.; Fukumura, D.; Jain, R. K. Photodynamic Therapy for Cancer. *Nat. Rev. Cancer* **2003**, *3*, 380–387.
4. Zhu, Z.; Tang, Z. W.; Phillips, J. A.; Yang, R. H.; Wang, H.; Tan, W. H. Regulation of Singlet Oxygen Generation Using Single-Walled Carbon Nanotubes. *J. Am. Chem. Soc.* **2008**, *130*, 10856–10857.
5. Celli, J. P.; Spring, B. Q.; Rizvi, I.; Evans, C. L.; Samkoe, K. S.; Verma, S.; Pogue, B. W.; Hasan, T. Imaging and Photodynamic Therapy: Mechanisms, Monitoring, and Optimization. *Chem. Rev.* **2010**, *110*, 2795–2838.
6. Master, A.; Livingston, M.; Sen Gupta, A. Photodynamic Nanomedicine in the Treatment of Solid Tumors: Perspectives and Challenges. *J. Controlled Release* **2013**, *168*, 88–102.
7. Cai, R. X.; Kubota, Y.; Shuin, T.; Sakai, H.; Hashimoto, K.; Fujishima, A. Induction of Cytotoxicity by Photoexcited TiO_2 Particles. *Cancer Res.* **1992**, *52*, 2346–2348.
8. Rozhkova, E. A.; Ulasov, I.; Lai, B.; Dimitrijevic, N. M.; Lesniak, M. S.; Rajh, T. A High-Performance Nanobio Photocatalyst for Targeted Brain Cancer Therapy. *Nano Lett.* **2009**, *9*, 3337–3342.
9. Kubota, Y.; Shuin, T.; Kawasaki, C.; Hosaka, M.; Kitamura, H.; Cai, R.; Sakai, H.; Hashimoto, K.; Fujishima, A. Photokilling of T-24 Human Bladder Cancer Cells with Titanium Dioxide. *Br. J. Cancer.* **1994**, *70*, 1107–1111.
10. Lagopati, N.; Kitsiou, P. V.; Kontos, A. I.; Venieratos, P.; Kotsopoulou, E.; Kontos, A. G.; Dionysiou, D. D.; Pispas, S.; Tsilibary, E. C.; Falaras, P. Photo-Induced Treatment of Breast Epithelial Cancer Cells Using Nanostructured Titanium Dioxide Solution. *J. Photochem. Photobiol., A* **2010**, *214*, 215–223.
11. Wang, C.; Cao, S.; Tie, X.; Qiu, B.; Wu, A.; Zheng, Z. Induction of Cytotoxicity by Photoexcitation of TiO_2 Can Prolong Survival in Glioma-Bearing Mice. *Mol. Biol. Rep.* **2011**, *38*, 523–530.
12. Feng, X. H.; Zhang, S. K.; Lou, X. Controlling Silica Coating Thickness on TiO_2 Nanoparticles for Effective Photodynamic Therapy. *Colloids Surf., B* **2013**, *107*, 220–226.
13. Zeng, L. Y.; Ren, W. Z.; Xiang, L. C.; Zheng, J. J.; Chen, B.; Wu, A. G. Multifunctional Fe_3O_4-TiO_2 Nanocomposites for Magnetic Resonance Imaging and Potential Photodynamic Therapy. *Nanoscale* **2013**, *5*, 2107–2113.
14. Zhang, H.; Shi, R. H.; Xie, A. J.; Li, J. C.; Chen, L.; Chen, P.; Li, S. K.; Huang, F. Z.; Shen, Y. H. Novel TiO_2/PEGDA Hybrid Hydrogel Prepared *in Situ* on Tumor Cells for Effective Photodynamic Therapy. *ACS Appl. Mater. Interfaces* **2013**, *5*, 12317–12322.
15. Oar, M. A.; Serin, J. M.; Dichtel, W. R.; Frechet, J. M. J.; Ohulchanskyy, T. Y.; Prasad, P. N. Photosensitization of Singlet Oxygen *via* Two-Photon-Excited Fluorescence Resonance Energy Transfer in a Water-Soluble Dendrimer. *Chem. Mater.* **2005**, *17*, 2267–2275.
16. Huang, Z.; Xu, H.; Meyers, A. D.; Musani, A. I.; Wang, L.; Tagg, R.; Barqawi, A. B.; Chen, Y. K. Photodynamic Therapy for Treatment of Solid Tumors-Potential and Technical Challenges. *Technol. Cancer Res. Treat.* **2008**, *7*, 309–320.
17. Wang, C.; Tao, H.; Cheng, L.; Liu, Z. Near-Infrared Light Induced *in Vivo* Photodynamic Therapy of Cancer Based on Upconversion Nanoparticles. *Biomaterials* **2011**, *32*, 6145–6154.
18. Shan, J. N.; Budijono, S. J.; Hu, G. H.; Yao, N.; Kang, Y. B.; Ju, Y. G.; Prud'homme, R. K. Pegylated Composite Nanoparticles

Containing Upconverting Phosphors and meso-Tetraphenyl porphine (TPP) for Photodynamic Therapy. *Adv. Funct. Mater.* **2011**, *21*, 2488–2495.
19. Liu, K.; Liu, X.; Zeng, Q.; Zhang, Y.; Tu, L.; Liu, T.; Kong, X.; Wang, Y.; Cao, F.; Lambrechts, S. A. G.; Aalders, M. C. G.; Zhang, H. Covalently Assembled NIR Nanoplatform for Simultaneous Fluorescence Imaging and Photodynamic Therapy of Cancer Cells. *ACS Nano* **2012**, *6*, 4054–4062.
20. Cui, S.; Yin, D.; Chen, Y.; Di, Y.; Chen, H.; Ma, Y.; Achilefu, S.; Gu, Y. *In Vivo* Targeted Deep-Tissue Photodynamic Therapy Based on Near-Infrared Light Triggered Upconversion Nanoconstruct. *ACS Nano* **2013**, *7*, 676–688.
21. Boulnois, J. L. Photophysical Processes in Recent Medical Laser Developments: A Review. *Lasers Med. Sci.* **1986**, *1*, 47–66.
22. Frangioni, J. V. *In Vivo* near-Infrared Fluorescence Imaging. *Curr. Opin. Chem. Biol.* **2003**, *7*, 626–634.
23. Heer, S.; Kompe, K.; Gudel, H. U.; Hasse, M. Highly Efficient Multicolour Upconversion Emission in Transparent Colloids of Lanthanide-Doped NaYF4 Nanocrystals. *Adv. Mater.* **2004**, *16*, 2102–2105.
24. Boyer, J. C.; Vetrone, F.; Cuccia, L. A.; Capobianco, J. A. Synthesis of Colloidal Upconverting $NaYF_4$ Nanocrystals Doped with Er^{3+}, Yb^{3+} and Tm^{3+}, Yb^{3+} *via* Thermal Decomposition of Lanthanide Trifluoroacetate Precursors. *J. Am. Chem. Soc.* **2006**, *128*, 7444–7445.
25. Nyk, M.; Kumar, R.; Ohulchanskyy, T. Y.; Bergey, E. J.; Prasad, P. N. High Contrast *in Vitro* and *in Vivo* Photoluminescence Bioimaging Using Near Infrared to Near Infrared Up-Conversion in Tm^{3+} and Yb^{3+} Doped Fluoride Nanophosphors. *Nano Lett.* **2008**, *8*, 3834–3838.
26. Ye, X. C.; Collins, J. E.; Kang, Y. J.; Chen, J.; Chen, D. T. N.; Yodh, A. G.; Murray, C. B. Morphologically Controlled Synthesis of Colloidal Upconversion Nanophosphors and Their Shape-Directed Self-Assembly. *Proc. Natl. Acad. Sci. U.S.A.* **2010**, *107*, 22430–22435.
27. Wang, H. Q.; Batentschuk, M.; Osvet, A.; Pinna, L.; Brabec, C. J. Rare-Earth Ion Doped Up-Conversion Materials for Photovoltaic Applications. *Adv. Mater.* **2011**, *23*, 2675–2680.
28. Hou, Z. Y.; Li, C. X.; Ma, P. A.; Cheng, Z. Y.; Li, X. J.; Zhang, X.; Dai, Y. L.; Yang, D. M.; Lian, H. Z.; Lin, J. Up-Conversion Luminescent and Porous $NaYF_4$:Yb^{3+}, Er^{3+}@SiO_2 Nanocomposite Fibers for Anti-Cancer Drug Delivery and Cell Imaging. *Adv. Funct. Mater.* **2012**, *22*, 2713–2722.
29. Gorris, H. H.; Wolfbeis, O. S. Photon-Upconverting Nanoparticles for Optical Encoding and Multiplexing of Cells, Biomolecules, and Microspheres. *Angew. Chem., Int. Ed.* **2013**, *52*, 3584–3600.
30. Mai, H. X.; Zhang, Y. W.; Si, R.; Yan, Z. G.; Sun, L. D.; You, L. P.; Yan, C. H. Glutathione- and Cysteine-Induced Transverse Overgrowth on Gold Nanorods. *J. Am. Chem. Soc.* **2006**, *128*, 6402–6404.
31. Chen, Z. G.; Chen, H. L.; Hu, H.; Yu, M. X.; Li, F. Y.; Zhang, Q.; Zhou, Z. G.; Yi, T.; Huang, C. H. Versatile Synthesis Strategy for Carboxylic Acid−Functionalized Upconverting Nanophosphors as Biological Labels. *J. Am. Chem. Soc.* **2008**, *130*, 3023–3029.
32. van der Ende, B. M.; Aarts, L.; Meijerink, A. Near-Infrared Quantum Cutting for Photovoltaics. *Adv. Mater.* **2009**, *21*, 3073–3077.
33. Zhang, F.; Braun, G. B.; Shi, Y. F.; Zhang, Y. C.; Sun, X. H.; Reich, N. O.; Zhao, D. Y.; Stucky, G. Fabrication of Ag@SiO_2@Y_2O_3:Er Nanostructures for Bioimaging: Tuning of the Upconversion Fluorescence with Silver Nanoparticles. *J. Am. Chem. Soc.* **2010**, *132*, 2850–2851.
34. Wang, F.; Han, Y.; Lim, C. S.; Lu, Y. H.; Wang, J.; Xu, J.; Chen, H. Y.; Zhang, C.; Hong, M. H.; Liu, X. G. Simultaneous Phase and Size Control of Upconversion Nanocrystals through Lanthanide Doping. *Nature* **2010**, *463*, 1061–1065.
35. Wang, G. F.; Peng, Q.; Li, Y. D. Lanthanide-Doped Nanocrystals: Synthesis, Optical-Magnetic Properties, and Applications. *Acc. Chem. Res.* **2011**, *44*, 322–332.
36. Liu, Y. S.; Tu, D. T.; Zhu, H. M.; Chen, X. Y. Lanthanide-Doped Luminescent Nanoprobes: Controlled Synthesis, Optical Spectroscopy, and Bioapplications. *Chem. Soc. Rev.* **2013**, *42*, 6924–6958.
37. Zhang, P.; Steelant, W.; Kumar, M.; Scholfield, M. Versatile Photosensitizers for Photodynamic Therapy at Infrared Excitation. *J. Am. Chem. Soc.* **2007**, *129*, 4526–4527.
38. Idris, N. M.; Gnanasammandhan, M. K.; Zhang, J.; Ho, P. C.; Mahendran, R.; Zhang, Y. *In Vivo* Photodynamic Therapy Using Upconversion Nanoparticles as Remote-Controlled Nanotransducers. *Nat. Med.* **2012**, *18*, 1580–1585.
39. Yuan, Q.; Wu, Y.; Wang, J.; Lu, D. Q.; Zhao, Z. L.; Liu, T.; Zhang, X. B.; Tan, W. H. Targeted Bioimaging and Photodynamic Therapy Nanoplatform Using an Aptamer-Guided G-Quadruplex DNA Carrier and Near-Infrared Light. *Angew. Chem., Int. Ed.* **2013**, *52*, 13965–13969.
40. Wang, C.; Cheng, L.; Liu, Y. M.; Wang, X. J.; Ma, X. X.; Deng, Z. Y.; Li, Y. G.; Liu, Z. Imaging-Guided pH-Sensitive Photodynamic Therapy Using Charge Reversible Upconversion Nanoparticles under Near-Infrared Light. *Adv. Funct. Mater.* **2013**, *23*, 3077–3086.
41. Idris, N. M.; Lucky, S. S.; Li, Z. Q.; Huang, K.; Zhang, Y. Photoactivation of Core-Shell Titania Coated Upconversion Nanoparticles and Its Effect on Cell Death. *J. Mater. Chem. B* **2014**, *2*, 7017–7026.
42. Yin, M. L.; Ju, E. G.; Chen, Z. W.; Li, Z. H.; Ren, J. S.; Qu, X. G. Upconverting Nanoparticles with a Mesoporous TiO_2 Shell for Near-Infrared-Triggered Drug Delivery and Synergistic Targeted Cancer Therapy. *Chem.—Eur. J.* **2014**, *20*, 14012–14017.
43. Juzenas, P.; Chen, W.; Sun, Y. P.; Coelho, M. A. N.; Generalov, R.; Generalova, N.; Christensen, I. L. Quantum Dots and Nanoparticles for Photodynamic and Radiation Therapies of Cancer. *Adv. Drug Delivery Rev.* **2008**, *60*, 1600–1614.
44. Lim, M. E.; Lee, Y. L.; Zhang, Y.; Chu, J. J. H. Photodynamic Inactivation of Viruses Using Upconversion Nanoparticles. *Biomaterials* **2012**, *33*, 1912–1920.
45. Tian, G.; Ren, W. L.; Yan, L.; Jian, S.; Gu, Z. J.; Zhou, L. J.; Jin, S.; Yin, W. Y.; Li, S. J.; Zhao, Y. L. Red-Emitting Upconverting Nanoparticles for Photodynamic Therapy in Cancer Cells under Near-Infrared Excitation. *Small* **2013**, *9*, 1929–1938.
46. Wang, M.; Chen, Z.; Zheng, W.; Zhu, H. M.; Lu, S.; Ma, E.; Tu, D. T.; Zhou, S. Y.; Huang, M. D.; Chen, X. Y. Lanthanide-Doped Upconversion Nanoparticles Electrostatically Coupled with Photosensitizers for Near-Infrared-Triggered Photodynamic Therapy. *Nanoscale* **2014**, *6*, 8274–8282.
47. Chen, Q.; C. Wang, C.; Cheng, L.; He, W. W.; Cheng, Z. P.; Liu, Z. Protein Modified Upconversion Nanoparticles for Imaging-Guided Combined Photothermal and Photodynamic Therapy. *Biomaterials* **2014**, *35*, 2915–2923.
48. Qin, W. P.; Zhang, D. S.; Zhao, D.; Wang, L. L.; Zheng, K. Z. Near-Infrared Photocatalysis Based on YF_3:Yb^{3+},Tm^{3+}/TiO_2 Core/Shell Nanoparticles. *Chem. Commun.* **2010**, *46*, 2304–2306.
49. Zhang, Y. W.; Hong, Z. L. Synthesis of Lanthanides-Doped $NaYF_4$@TiO_2 Core/Shell Composites with Highly Crystallized and Controllable TiO_2 Shell under Mild Conditions and Their Upconversion-Based Photocatalysis. *Nanoscale* **2014**, *5*, 8930–8933.
50. Li, Z. Q.; Li, C. L.; Mei, Y. Y.; Wang, L. M.; Du, G. H.; Xiong, Y. J. Synthesis of Rhombic Hierarchical YF3 Nanocrystals and Their Use as Upconversion Photocatalysts after TiO_2 Coating. *Nanoscale* **2013**, *5*, 3030–3036.
51. Su, W. K.; Zheng, M. M.; Li, L.; Wang, K.; Qiao, R.; Zhong, Y. J.; Hu, Y.; Li, Z. G. Directly Coat TiO_2 on Hydrophobic $NaYF_4$:Yb,Tm Nanoplates and Regulate Their Photocatalytic Activities with the Core Size. *J. Mater. Chem. A* **2014**, *2*, 13486–13491.
52. Goodgame, D. M. L.; Williams, D. J.; Winpenny, R. E. P. $[(Hg_3Co(C_4H_6NO)_6)(NO_3)_2]_n$: A Macrobicyclic Bimetallic Chain Polymer Incorporating Deprotonated 2-Pyrrolodone Bridges. *Angew. Chem., Int. Ed.* **1988**, *100*, 261–262.
53. Li, Q.; Li, T.; Wu, J. G. Luminescence of Europium(III) and Terbium(III) Complexes Incorporated in Poly(vinyl pyrrolidone) Matrix. *J. Phys. Chem. B* **2001**, *105*, 12293–12296.
54. Meng, F. X.; Liu, S.; Wang, Y. F.; Tao, C.; Xu, P.; Guo, W. B.; Shen, L.; Zhang, X. D.; Ruan, S. P. Open-Circuit Voltage

Enhancement of Inverted Polymer Bulk Heterojunction Solar Cells by Doping NaYF4 Nanoparticles/PVP Composites. *J. Mater. Chem.* **2012**, *22*, 22382–22386.
55. Yang, Y.; Li, J. R.; Mu, J. H.; Rong, L.; Jiang, L. A Gold Nanocomposite Made Soluble in Both Water and Oil by the Addition of a Second Adsorption Layer of Poly-N-vinyl-2-pyrrolidone on Gold Nanoparticles that Have Been Made Hydrophobic. *Nanotechnology* **2006**, *17*, 461–465.
56. Li, Z. Q.; Zhang, Y. Monodisperse Silica-Coated Polyvinylpyrrolidone/$NaYF_4$ Nanocrystals with Multicolor Upconversion Fluorescence Emission. *Angew. Chem., Int. Ed.* **2006**, *45*, 7732–7735.
57. Cha, J. Y.; Cui, P.; Lee, J. K. A Simple Method to Synthesize Multifunctional Silica Nanocomposites, NPs@SiO_2, Using Polyvinylpyrrolidone (PVP) as a Mediator. *J. Mater. Chem.* **2010**, *20*, 5533–5537.
58. Lou, X. W.; Archer, L. A. A General Route to Nonspherical Anatase TiO_2 Hollow Colloids and Magnetic Multifunctional Particles. *Adv. Mater.* **2008**, *20*, 1853–1858.
59. Qin, W. P.; Zhang, D. S.; Zhao, D.; Wang, L. L.; Zheng, K. Z. Near-Infrared Photocatalysis Based on YF_3:Yb^{3+},Tm^{3+}/TiO_2 Core/Shell Nanoparticles. *Chem. Commun.* **2010**, *46*, 2304–2306.
60. Xu, D. X.; Lian, Z. W.; Fu, M. L.; Yuan, B. L.; Shi, J. W.; Cui, H. J. Advanced Near-Infrared-Driven Photocatalyst: Fabrication, Characterization, and Photocatalytic Performance of β-$NaYF_4$:Yb^{3+},Tm^{3+}@TiO_2 Core@Shell Microcrystals. *Appl. Catal. B: Environ.* **2013**, *142−143*, 377–386.
61. Zhang, Y. W.; Hong, Z. L. Synthesis of Lanthanides-Doped $NaYF_4$@TiO_2 Core/Shell Composites with Highly Crystallized and Controllable TiO_2 Shell under Mild Conditions and Their Upconversion-Based Photocatalysis. *Nanoscale* **2014**, *5*, 8930–8933.
62. Zhang, H. J.; Shan, Y. F.; Dong, L. J. A Comparison of TiO_2 and ZnO Nanoparticles as Photosensitizers in Photodynamic Therapy for Cancer. *J. Biomed. Nanotechnol.* **2014**, *10*, 1450–1457.
63. Han, L.; Du, L. B.; Kumar, A.; Jia, H. Y.; Liang, X. J.; Tian, Q.; Nie, G. J. Inhibitory Effects of Trolox-Encapsulated Chitosan Nanoparticles on Tert-Butylhydroperoxide Induced RAW264.7 Apoptosis. *Biomaterials* **2012**, *33*, 8517–8528.
64. Wang, L.; Lu, K. Y.; Hao, H. H.; Li, X. Y.; Wang, J.; Wang, K.; Wang, J.; Yan, Z.; Zhang, S. L.; Du, Y. H.; Liu, H. R. Decreased Autophagy in Rat Heart Induced by Anti-beta 1-Adrenergic Receptor Autoantibodies Contributes to the Decline in Mitochondrial Membrane Potential. *PLoS One* **2013**, *8*, e81296.
65. Cavalieri, E.; Rigo, A.; Bonifacio, M.; De Prati, A. C.; Guardalben, E.; Bergamini, C.; Fato, R.; Pizzolo, G.; Suzuki, H.; Vinante, F. Pro-Apoptotic Activity of Alpha-Bisabolol in Preclinical Models of Primary Human Acute Leukemia Cells. *J. Transl. Med.* **2011**, *9*, 45.
66. Shin, Y. S.; Shin, H. A.; Kang, S. U.; Kim, J. H.; Oh, Y. T.; Park, K. H.; Kim, C. H. Effect of Epicatechin against Radiation-Induced Oral Mucositis: *in Vitro* and *in Vivo* Study. *PLoS One* **2013**, *8*, e69151.
67. Daniel, P. T.; Schulze-Osthoff, K.; Belka, C.; Guner, D. Guardians of Cell Death: the Bcl-2 Family Proteins. *Essays Biochem.* **2003**, *39*, 73–88.
68. Reed, J. C. Bcl-2 Family Proteins: Regulators of Apoptosis and Chemoresistance in Hematologic Malignancies. *Semin. Hematol.* **1997**, *34*, 9–19.
69. Kirkin, V.; Joos, S.; Zornig, M. The Role of Bcl-2 Family Members in Tumorigenesis. *Biochim. Biophys. Acta* **2004**, *1644*, 229–249.
70. Hsiao, C. J.; Hsiao, G.; Chen, W. L.; Wang, S. W.; Chiang, C. P.; Liu, L. Y.; Guh, J. W.; Lee, T. H.; Chung, C. L. Cephalochromin Induces G0/G1 Cell Cycle Arrest and Apoptosis in A549 Human Non-Small-Cell Lung Cancer Cells by Inflicting Mitochondrial Disruption. *J. Nat. Prod.* **2014**, *77*, 758–765.
71. Griffiths, G. J.; Dubrez, L.; Morgan, C. P.; Jones, N. A.; Whitehouse, J.; Corfe, B. M.; Dive, C.; Hickman, J. A. Cell Damage Induced Conformational Changes of the Pro-Apoptotic Protein Bak *in Vivo* Precede the Onset of Apoptosis. *J. Cell Biol.* **1999**, *144*, 903–914.
72. Wei, M. C.; Lindsten, T.; Mootha, V. K.; Weiler, S.; Gross, A.; Ashiya, M.; Thompson, C. B.; Korsmeyer, S. J. tBID, a Membrane-Targeted Death Ligand, Oligomerizes BAK to Release Cytochrome C. *Genes Dev.* **2000**, *14*, 2060–2071.
73. Wei, M. C.; Zong, W. X.; Cheng, E. H.; Lindsten, T.; Panoutsakopoulou, V.; Ross, A. J.; Roth, K. A.; MacGregor, G. R.; Thompson, C. B.; Korsmeyer, S. J. Proapoptotic BAX and BAK: a Requisite Gateway to Mitochondrial Dysfunction and Death. *Science* **2001**, *292*, 727–730.
74. Yu, C. H.; Chen, H. M.; Lin, H. P.; Chiang, C. P. Expression of Bak and Bak/Mcl-1 Ratio Can Predict Photodynamic Therapy Outcome for Oral Verrucous Hyperplasia and Leukoplakia. *J. Oral. Pathol. Med.* **2013**, *42*, 257–262.
75. Chen, H. M.; Yu, C. H.; Lin, H. P.; Cheng, S. J.; Chiang, C. P. 5-Aminolevulinic Acid-Mediated Photodynamic Therapy for Oral Cancers and Precancers. *J. Dent. Sci.* **2012**, *7*, 307–315.
76. Frank, J. C.; Plötz, M.; Prokop, A.; Geilen, C. C.; Schmalz, H. G.; Eberle, J. New Caspase-Independent but ROS-Dependent Apoptosis Pathways Are Targeted in Melanoma Cells by an Iron-Containing Cytosine Analogue. *Biochem. Pharmacol.* **2010**, *79*, 575–586.
77. Chen, C.; Hu, S. Y.; Luo, D. Q.; Zhu, S. Y.; Zhou, C. Q. Potential Antitumor Agent from the Endophytic Fungus Pestalotiopsis Photiniae Induces Apoptosis *via* the Mitochondrial Pathway in HeLa Cells. *Oncol. Rep.* **2013**, *30*, 1773–1781.
78. Zhang, Y. Q.; Xiao, C. X.; Lin, B. Y.; Shi, Y.; Liu, Y. P.; Liu, J. J.; Guleng, B.; Ren, J. L. Silencing of Pokemon Enhances Caspase-Dependent Apoptosis *via* Fas- and Mitochondria-Mediated Pathways in Hepatocellular Carcinoma Cells. *PLoS One* **2013**, *8*, e68981.
79. Agostinis, P.; Buytaert, E.; Breyssens, H.; Hendrickx, N. Regulatory Pathways in Photodynamic Therapy Induced Apoptosis. *Photochem. Photobiol. Sci.* **2004**, *3*, 721–729.
80. Zhang, Y. X.; Li, Q. S.; Ge, Y. K.; Chen, Y. P.; Chen, J.; Dong, Y.; Shi, W. Silibinin Triggers Apoptosis and Cell-Cycle Arrest of SGC7901 Cells. *Phytother. Res.* **2013**, *27*, 397–403.
81. Oleinick, N. L.; Morris, R. L.; Belichenko, I. The Role of Apoptosis in Response to Photodynamic Therapy: What, Where, Why, and How. *Photochem. Photobiol. Sci.* **2002**, *1*, 1–21.
82. Castano, A. P.; Demidova, T. N.; Hamblin, M. R. Mechanisms in Photodynamic Therapy: Part Two-Cellular Signaling, Cell Metabolism and Modes of Cell Death. *Photodiagn. Photodyn. Ther.* **2005**, *2*, 1–23.
83. Zhao, H. Y.; Yin, R.; Chen, D. Y.; Ren, J.; Wang, Y. C.; Zhang, J. Y.; Deng, H.; Wang, Y.; Qiu, H. X.; Huang, N. Y.; Zou, Q. L.; Zhao, J. Q.; Gu, Y. *In Vitro* and *in Vivo* Antitumor Activity of a Novel Hypocrellin B Derivative for Photodynamic Therapy. *Photodiagn. Photodyn. Ther.* **2014**, *11*, 204–212.
84. Almeida, R. D.; Manadas, B. J.; Casvalho, A. P.; Duarte, C. B. Intracellular Signaling Mechanisms in Photodynamic Therapy. *Biochim. Biophys. Acta* **2004**, *1704*, 59–86.
85. Buytaert, E.; Devaele, M.; Agostinis, P. Molecular Effectors of Multiple Cell Death Pathways Initiated by Photodynamic Therapy. *Biochim. Biophys. Acta* **2007**, *1776*, 86–107.
86. Agrawal, S. S.; Saraswati, S.; Mathur, R.; Pandey, M. Cytotoxic and Antitumor Effects of Brucine on Ehrlich Ascites Tumor and Human Cancer Cell Line. *Life Sci.* **2011**, *89*, 147–158.
87. Xue, M. L.; Ge, Y. L.; Zhang, J. Y.; Wang, Q.; Hou, L.; Liu, Y. C.; Sun, L. L.; Li, Q. Anticancer Properties and Mechanisms of Fucoidan on Mouse Breast Cancer *in Vitro* and *in Vivo*. *PLoS One* **2012**, *7*, e43483.
88. Maheshwari, A.; Misro, M. M.; Aggarwal, A.; Sharma, R. K. N-Acetyl-L-cysteine Modulates Multiple Signaling Pathways to Rescue Male Germ Cells from Apoptosis Induced by Chronic hCG Administration to Rats. *Apoptosis* **2012**, *17*, 551–565.
89. Yu, W.; Zha, W. L.; Guo, S.; Cheng, H. K.; Wu, J. L.; Liu, C. Flos Puerariae Extract Prevents Myocardial Apoptosis *via* Attenuation Oxidative Stress in Streptozotocin-Induced Diabetic Mice. *PLoS One* **2014**, *9*, e98044.
90. Park, Y. I.; Kim, H. M.; Kim, J. H.; Moon, K. C.; Yoo, B.; Lee, K. T.; Lee, N.; Choi, Y.; Park, W.; Ling, D.; Na, K.; Moon, W. K.; Choi,

S. H.; Park, H. S.; Yoon, S.-Y.; Suh, Y. D.; Lee, S. H.; Hyeon, T. Theranostic Probe Based on Lanthanide-Doped Nanoparticles for Simultaneous *in Vivo* Dual-Modal Imaging and Photodynamic Therapy. *Adv. Mater.* **2012**, *24*, 5755–5761.
91. Hou, Z. Y.; Li, C. X.; Ma, P. A.; Li, G. G.; Cheng, Z. Y.; Peng, C.; Yang, D. M.; Yang, P. P.; Lin, J. Electrospinning Preparation and Drug-Delivery Properties of an Up-conversion Luminescent Porous $NaYF_4$:Yb^{3+}, Er^{3+}@Silica Fiber Nanocomposite. *Adv. Funct. Mater.* **2011**, *21*, 2356–2365.
92. Wang, G. F.; Peng, Q.; Li, Y. D. Lanthanide-Doped Nanocrystals: Synthesis, Optical-Magnetic Properties, and Applications. *Acc. Chem. Res.* **2011**, *44*, 322–332.
93. Li, C. X.; Yang, D. M.; Ma, P. A.; Chen, Y. Y.; Wu, Y.; Hou, Z. Y.; Dai, Y. L.; Zhao, J. H.; Sui, C. P.; Lin, J. Multifunctional Upconversion Mesoporous Silica Nanostructures for Dual Modal Imaging and *in Vivo* Drug Delivery. *Small* **2013**, *9*, 4150–4159.